

Chapter 1: Introduction

Bose statistics were first developed in 1924 to describe the quantum behavior of photons [1], quanta of light with integer-valued spin. Today, we routinely produce atomic Bose-Einstein condensates in the laboratory and even use them as a platform for the analog simulation of complex systems. The field has certainly come a long way!

Bose-Einstein condensation (BEC) in atomic gases was observed for the first time in 1995 in dilute vapors of ^{87}Rb [2] and ^{23}Na [3]. Even though the BEC phase had been predicted for a long time it wasn't until experimental techniques of laser cooling and trapping [4] were developed that bosonic atoms were cooled down to temperatures low enough for condensation to occur¹. The experimental realization of this new phase of matter opened new possibilities for studying macroscopic quantum phenomena such as the propagation of collective modes [5, 6] and interference of coherent matter waves [7] and jump-started an ever-growing field of research. For this achievement, Eric Cornell, Carl Wieman, and Wolfgang Ketterle were awarded the 2001 Nobel Prize in physics.

It has been more than 20 years (and many more in the learning of atomic

¹For a more in depth story of the BEC field I highly recommend reading [4].

physics) and the field of quantum degenerate gases has expanded to include degenerate Fermi gases [8] and spinor gases [9]. As the field continues to grow, new control and detection techniques are ~~being constantly developed~~, enabling the use of BECs and ultracold atomic systems in general not just as an object of study by themselves but as tools for a wide range of scientific endeavors, from precision measurements [10] to the analog simulation of complex systems.

Quantum degenerate gases ~~have proven to be~~ an ideal platform for quantum simulation [11]. A ~~very~~ straightforward example comes from the use of optical lattices, where the periodic potential imparted by standing waves of light serves as an analogue to the crystal structure in a solid. Perhaps the first iconic realization of a quantum simulation was the study of the Bose-Hubbard model in three-dimensional optical lattices [12], the bosonic analogue of a model which is believed to be relevant to high- T_c superconductors.

The development of light-induced gauge-fields [13] has been another important milestone in the field of quantum simulation. Such fields can be used to mimic the effect of magnetic [14, 15] and electric [16] fields with potential applications to the realization of quantum Hall materials with large magnetic fluxes [14, 17] and fractional quantum Hall states [18]. Furthermore, light-induced gauge fields can be used to engineer spin-orbit coupling interactions [19] as those present in two-dimensional materials, a necessary ingredient for the spin quantum Hall effect and certain kinds of topological insulators [20]. Chapter 8 will focus on a new implementation of Rashba-type spin-orbit [21, 22] coupling in ~~an~~-ultracold ^{87}Rb atoms.

The precise level of control and tunability of ultracold atomic systems allow us to readily implement important physical models in the laboratory. Furthermore, we can go beyond conventional materials existing in nature, and ~~thereby~~ create new exotic atomic ‘materials’, with interaction-dominated or topologically non-trivial band structures that can help deepen our understanding of the physical consequences of these effects on materials.

This thesis focuses on the development of new tools for the characterization and control of engineered quantum and applies them to create and characterize a topological system with Rashba-type spin-orbit coupling.

The creation of new engineered materials requires the ability to characterize their single particle energies. We developed a Fourier transform spectroscopy technique which allows us to probe the single particle spectrum, and ~~thereby~~ verify our quantum engineering, by only looking ~~at~~ quantum coherent evolution.

Atomic systems are susceptible ~~to environmental noise~~, leading to undesired effects such as the loss of coherence. In particular laboratories such as ours greatly suffer from noise in ambient magnetic fields and go through great efforts to diminish their effects. We implemented continuous dynamical decoupling (CDD) on a set of internal atomic states which renders them first order insensitive~~to~~ magnetic field changes, effectively turning them into clock states. These CDD states are not just a robust basis for performing experiments, they additionally gave us access to new matrix elements which were essential for the engineering of the Rashba Hamiltonian as well as other novel lattice systems [23] not presented in this thesis.

The engineering of Rashba spin-orbit coupling is ~~certainly~~ condensed matter

inspired. However, part of the beauty of engineered quantum systems is we can depart from conventional materials, for example, by considering a system with Rashba SOC but without an underlying crystalline structure. We do so in the last part of this thesis and find that our conventional understanding of the topology of Bloch bands is defied by measuring half-integer valued topological invariants.

1.1 Thesis overview

This thesis describes both the standard experimental control and measurement techniques used to create BECs of ^{87}Rb as well as new techniques developed in our ~~lab that were applied to~~ the engineering of Rashba spin-orbit coupling.

Chapter 2 describes the basic theory of Bose-Einstein condensation in dilute gases. I focus on the properties of gases confined to harmonic potentials and their density and momentum distributions as they are most relevant to the experiments presented here.

Chapter 3 describes the ~~basic~~ properties of Alkali atoms and their interactions with magnetic and electric fields which are used as standard tools for the creation, manipulation and detection of ultracold atomic systems.

Chapter 4 summarizes the experimental apparatus ~~where all the experiments were performed~~. It ~~additionally~~ mentions the most important upgrades to the apparatus ~~that were not reported previously~~.

Chapter 5 describes a Fourier transform spectroscopy technique that exploits the relation between quantum coherent evolution and the underlying spectrum of a

system and that was used to characterize experiments described later in the thesis.

Chapter 6 describes an implementation of continuous dynamical decoupling using a strong radio-frequency magnetic field that helped to both make our system more robust against environmental magnetic field ~~noise and also allowed~~ us to couple the internal states of the atoms in new ways that were not possible before, opening the path for new kinds of quantum simulations described in Chapters 8.

Chapter 7 presents ~~basic~~ concepts of topology in physics and its application to the band theory of solids. These concepts will be important for a better understanding of the topological properties of our Rashba spin-orbit coupled system.

Chapter 8 ~~I~~-describes a new experimental realization of Rashba spin-orbit coupling using a combination of laser beams that couple a set of CDD states. ~~The~~ system ~~described in this chapter~~ has a topological dispersion relation but no underlying crystalline structure which allows for topological invariants to take non-integer values.

Chapter 2: Overview of Bose-Einstein condensation

Bose-Einstein condensation (BEC) is a quantum state of matter in which particles with integer valued spin all tend to occupy or ‘condense’ into the ground state. In dilute gases, condensation occurs when the temperature of the system goes below a critical temperature where the bosons become indistinguishable particles and quantum statistics become relevant.

BECs enable the ~~observation~~ of macroscopic quantum phenomena ~~and there~~ have been a number of fascinating experiments studying the properties of these systems, from measuring interference fringes of a macroscopic wave function to studying collective effects such as the propagation of sound [4], ~~as well as extensive theoretical developments~~ [24]. In our experiments however BECs are not the primary object of study, instead, they are used as a platform enabling the simulation of analog physical systems.

~~In this Chapter I give an overview of Bose-Einstein condensation in dilute atomic gases and I describe the properties most relevant to our experiments. I start by describing the case of an ideal gas and then consider the effects of interactions and trapping potentials as are present in our case. A reader interested in learning about this subject in more depth is advised to read [25] and [26].~~

2.1 Bose-Einstein condensation of an ideal gas

At low temperatures and in thermodynamic equilibrium, the mean occupation number of non-interacting identical bosons in the state with energy E is given by the Bose-Einstein distribution

$$n(E_j) = \frac{1}{e^{(E_j - \mu)/k_B T} - 1} \quad (2.1)$$

where T is the temperature, μ is the chemical potential (the energy cost of adding or removing a particle) and k_B is the Boltzmann constant. In the limit of large temperatures the Bose distribution can be approximated by the Maxwell-Boltzmann distribution

$$n(E_j) \approx e^{-(E_j - \mu)/kT} \quad (2.2)$$

which applies to classical, distinguishable particles. The chemical potential is determined by the condition that the total number of particles N is equal to the sum over all states in the distribution $N = \sum_j n(E_j)$ and is therefore a function of N and T . Additionally, in order for $n(E_j)$ to be positive definite we must have $\mu \leq E_0$ where E_0 is the energy of the ground state. From the Bose distribution, we can see that the occupation number of the ground state is unbounded when $\mu \rightarrow 0$ as is shown in Figure 2.1. The number of particles occupying the excited states is bounded and when that number is reached, the remaining particles can occupy the ground state and thus Bose-Einstein condensation occurs.

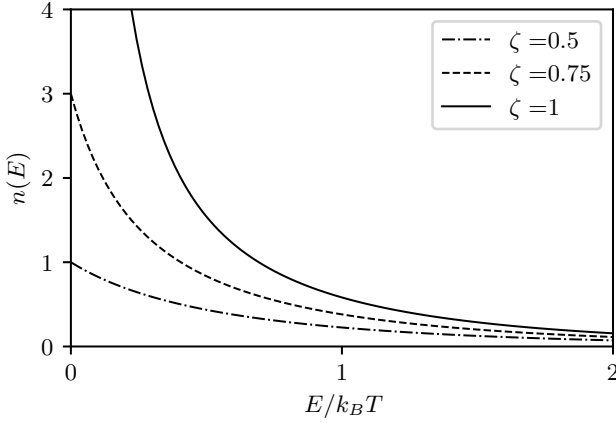


Figure 1: The Bose-Einstein distribution. Occupation number as a function of energy for different values of fugacity $\zeta = \exp(\mu/k_B T)$. Condensation occurs when $\mu = 0$ ($\zeta = 1$) and the occupation number in the ground state diverges.

2.1.1 Critical temperature

Bose-Einstein condensation can be understood in terms of the de Broglie waves associated with particles. The thermal de Broglie wavelength is ~~defined as~~

$$\lambda_{\text{th}} = \left(\frac{2\pi\hbar^2}{mk_B T} \right)^{1/2} \quad (2.3)$$

and it ~~characterized~~ the spatial extension of the wave packet an individual particle at temperature T . Condensation occurs when λ_{th} becomes comparable with the inter-particle separation $n^{-1/3}$, where $n = N/V$. The quantity $n\lambda_{\text{th}}^3$ is known as the phase space density which describes the number of particles contained in a box with volume λ_{th}^3 .

An analytical expression for the critical temperature at which atoms condense can be derived using the Bose-Einstein distribution. For closely spaced energy lev-

els (compared to $k_B T$) the sum representing the total number of particles can be replaced by the integral

$$N = \int_0^\infty n(E)g(E)dE \quad (2.4)$$

where $g(E)$ is the density of states and $g(E)dE$ corresponds to the number of available states with energy between E and $E+dE$. For a free particle in three dimensions the density of states is

$$g(E) = \frac{Vm^{3/2}}{\sqrt{2\pi^2\hbar^2}} E^{1/2}, \quad (2.5)$$

and in general the density of states can be expressed as a power of energy $g(E) = C_\alpha E^{\alpha-1}$.

The integral in Equation 2.4 is not analytically solvable, however, we can make the simplifying assumption $\mu = 0$. The critical temperature T_c is determined by the condition that all particles are in the excited states

$$\begin{aligned} N &= N_{\text{ex}}(T_c, \mu = 0) \\ &= \int_0^\infty \frac{g(E)dE}{e^{E/k_B T_c} - 1} \\ &= C_\alpha (k_B T_c)^\alpha \int_0^\infty \frac{x^{\alpha-1}}{e^x - 1} \\ &= c_\alpha (k_B T_c)^\alpha \Gamma(\alpha) \zeta(\alpha) \end{aligned} \quad (2.6)$$

where I made the substitution $x = E/k_B T_c$, $\Gamma(\alpha) = \int_0^\infty x^{\alpha-1} e^{-x} dx$ is the Gamma function and $\zeta(\alpha) = \sum_{n=1}^\infty n^{-\alpha}$ is the Riemann zeta function. From Equation 2.6 we

find that the critical temperature for Bose-Einstein condensation is

$$k_B T_c = \left(\frac{N}{C_\alpha \Gamma(\alpha) \zeta(\alpha)} \right)^{1/\alpha}. \quad (2.7)$$

If we compute the phase space density for free particles in 3D with density of states given by Equation 2.5 in combination with the expression for the critical temperature (Equation 2.6) we find that ~~indeed~~ when $T = T_c$

$$n \lambda_{\text{th}}^3 = \zeta \left(\frac{3}{2} \right) \approx 2.612, \quad (2.8)$$

the inter-particle spacing and the thermal wavelength are comparable. In order to experimentally produce BECs, a combination of laser and evaporative cooling techniques are deployed such that we can increase the density while minimizing the temperature and ~~therefore~~ maximize the phase space density. The densities for BECs of Alkali atoms typically range ~~in of order~~ 10^{13} to 10^{15} atoms/cm⁻³.

2.1.2 Condensate fraction

~~Now we look at the fraction of particles occupying the ground state at temperatures below T_c . The total number of particles is given by $N = N_0 + N_{\text{ex}}$ the number of particles in the excited state will be given by the integral in Equation 2.4. For $g(E) = C_\alpha E^{\alpha-1}$ and $\alpha > 0$ the integral converges, we can then evaluate the integral~~

in Equation 2.6 for $T < T_c$ and get

$$\begin{aligned} N_{\text{ex}} &= c_\alpha (k_B T)^\alpha \Gamma(\alpha) \zeta(\alpha) \\ &= N \left(\frac{T}{T_c} \right)^\alpha, \end{aligned} \quad (2.9)$$

where I used the fact that when $T = T_c$ the total number $N = N_{\text{ex}}$. The number of particles in the ground state is therefore

$$\begin{aligned} N_0 &= N - N_{\text{ex}} \\ &= N \left[1 - \left(\frac{T}{T_c} \right)^\alpha \right] \end{aligned} \quad (2.10)$$

2.1.3 Bose gas in a harmonic trapping potential

I consider the particular case of particles confined in a three-dimensional harmonic potential

$$V(\mathbf{r}) = \frac{m}{2} (\omega_x^2 x^2 + \omega_y^2 y^2 + \omega_z^2 z^2) \quad (2.11)$$

as it is the most relevant to our experiments that are performed in optical dipole traps that can be described as harmonic potentials. The density of states for is

$$g(E) = \frac{E^2}{2\hbar^2 \omega_x \omega_y \omega_z}, \quad (2.12)$$

which corresponds to $\alpha = 3$ and $C_3 = (2\hbar^3\omega_x\omega_y\omega_z)^{-1}$. Using Equation 2.6, we find that the transition temperature is

$$k_B T_c = \frac{\hbar\bar{\omega}N^{1/3}}{\zeta(3)^{1/3}} \approx 0.94\hbar\bar{\omega}N^{1/3} \quad (2.13)$$

where $\bar{\omega} = (\omega_x\omega_y\omega_z)^{1/3}$ is the geometric mean of the oscillation frequencies. Similarly we find that the condensed fraction is

$$N_0 = N \left[1 - \left(\frac{T}{T_c} \right)^3 \right] \quad (2.14)$$

Condensates in harmonic traps have some striking features that will be further explored in more detail in the following sections. The confining potential makes the BECs both finite-sized and inhomogeneous which means that the BEC can be observed both in momentum space and in coordinate space. Another consequence of the inhomogeneity of these systems is the role of two-body interactions, which gets enhanced and leads to noticeable effects in measurable quantities [24, 27] such as interaction driven expansion when they are released from the confining potential. Some of these features will be discussed in more detail in the following sections.

2.2 Bose-Einstein condensation with atomic interactions

Even though atomic BECs are made from very dilute gases, the system is far from being an ideal gas and interactions need to be taken into account for a complete treatment.



The collisional properties of particles at low energies, such as cold atoms in a condensate, are dominated by *s*-wave scattering which can be described in terms of a single parameter the scattering length a that determines both the scattering cross-section $\sigma = 4\pi a^2$ and the phase shift of the scattered wave function.

The magnitude of the scattering length is determined by the interatomic interaction potentials. For Alkali atoms at large distances, the two-body interactions are dominated by an attractive Van der walls interaction $U(r) = -C_6/r^6$ that arises from dipole-dipole interactions. At smaller distances, the attractive potential is replaced by a strong repulsive electron-exchange interaction $U(r) \rightarrow \infty$. This minimal model captures the most important properties of the inter-atomic potential and can be solved analytically [28].

If the range of the interaction is much shorter than the mean inter-atomic distance the interaction can be approximated by an effective pseudo-potential $U_{\text{eff}}(\mathbf{r} - \mathbf{r}')$ such that

$$a = \frac{m}{4\pi\hbar^2} \int U_{\text{eff}}(\mathbf{r} - \mathbf{r}') d\mathbf{r} \quad (2.15)$$

which determines

$$U_{\text{eff}}(\mathbf{r} - \mathbf{r}') = \frac{4\pi\hbar^2 a}{m} \delta(\mathbf{r} - \mathbf{r}') = g\delta(\mathbf{r} - \mathbf{r}'). \quad (2.16)$$

This is a nice approximation as it allows us to model the scattering between atoms as a hard-sphere scattering process instead of considering the more complicated inter-atomic potentials. The sign of the scattering length determines the attractive or

repulsive nature of the interactions and it plays an important role in the experimental production of BECs as it determines the rate at which atoms thermalize during evaporative cooling.

2.2.1 Gross-Pitaevskii equation

The full Hamiltonian describing N identical bosons with contact interactions can be written as

$$\hat{H} = \sum_{i=1}^N \left[\frac{\mathbf{p}_i^2}{2m} + V(\mathbf{r}_i) \right] + g \sum_{i < j} \delta(\mathbf{r}_i - \mathbf{r}_j), \quad (2.17)$$

where $V(\mathbf{r})$ is an external potential and $\mathbf{p}_i = -i\hbar\nabla_i$ is the momentum. We now consider a normalized eigenstate of the Hamiltonian $\Psi(\mathbf{r}_1, \mathbf{r}_2, \dots, \mathbf{r}_N)$ that satisfies the Schrödinger equation. We can simplify this state by taking a mean field approach; we assume that the system has undergone condensation so that the majority of the particles share the same single particle ground state $\phi(\mathbf{r})$ the wavefunction can be approximated by a symmetrized product

$$\Psi(\mathbf{r}_1, \mathbf{r}_2, \dots, \mathbf{r}_N) = \prod_{i=1}^N \phi(\mathbf{r}_i), \quad (2.18)$$

where ϕ is normalized to unity. The energy of the state from Equation 2.18 is given by the expectation value

$$E = \int \Psi^* \hat{H} \Psi d\mathbf{r} \\ = N \int \phi^*(\mathbf{r}) \left[-\frac{\hbar^2}{2m} \nabla^2 + V(\mathbf{r}) + \frac{(N-1)}{2} g |\phi(\mathbf{r})|^2 \right] \phi(\mathbf{r}) d\mathbf{r}, \quad (2.19)$$

where $N(N-1)/2 \approx N^2/2$ counts the number of terms in the interaction energy.

~~Now we introduce~~ the wave function of the condensate $\psi(\mathbf{r}) = N^{1/2} \phi(\mathbf{r})$, ~~which when~~ inserted in Equation 2.19 makes the N factors cancel out. The optimal form of ψ should minimize the energy ~~subject to the normalization condition~~ $N = \int |\psi(\mathbf{r})|^2 d\mathbf{r}$.

~~This can be done by introducing a Lagrange multiplier μ so that~~

$$\frac{\delta}{\delta \psi^*(\mathbf{r})} \left(E - \mu \int |\psi|^2 d\mathbf{r} \right) = \left[-\frac{\hbar^2}{2m} \nabla^2 + V(\mathbf{r}) + g |\psi(\mathbf{r})|^2 - \mu \right] \psi(\mathbf{r}) = 0, \quad (2.20)$$

and we ~~thus~~ find that the condensate wave function obeys a non-linear Schrödinger equation known as the Gross-Pitaevskii (GP) equation.

$$\left[-\frac{\hbar^2}{2m} \nabla^2 + V(\mathbf{r}) + g |\psi(\mathbf{r})|^2 \right] \psi(\mathbf{r}) = \mu \psi(\mathbf{r}) \quad (2.21)$$

where μ plays the role of the chemical potential. The dynamics of the condensate will similarly be described by the time-dependent GP equation

$$i\hbar \frac{\partial}{\partial t} \psi(\mathbf{r}, t) = \left[-\frac{\hbar^2}{2m} + V(\mathbf{r}) + g |\psi(\mathbf{r}, t)|^2 \right] \psi(\mathbf{r}, t) \quad (2.22)$$

The GP equation is useful for describing the relevant phenomena associated with BECs, for example, the propagation of collective excitations and the expansion of the condensate when released from a trap. The crucial assumption when deriving these equations was the mean field approximation which should be valid for dilute BECs in which the condensate fraction is close to unity. The excitations of the system can be described by a set of equations similar to those of classical hydrodynamics derived from the GP equation or alternatively using Bogoliubov theory for weakly interacting bosons [25].

2.2.2 Multiple component BECs

So far the discussion has been limited to single component BECs but most of our experiments are performed using a combination of multiple atomic internal states. In general, for a multiple component condensate the scattering lengths characterizing the interactions depend on the internal states of the incoming and outgoing scattering channels. Two spin- f^1 particles colliding particles will be characterized by $2f$ scattering lengths a_F . For bosons the total spin F takes even values and in particular for ^{87}Rb atoms in the $f = 1$ hyperfine ground state there are two scattering lengths a_0 and a_2 corresponding to the two-particle total angular momentum states of $F = 0$ and $F = 2$ respectively. The values of scattering lengths are $a_0 = 101.8a_0$ and $a_2 = 100.4a_0$ [9] where $a_0 = 5.29 \times 10^{-11}$ is the Bohr radius. From

¹Here I use the symbol f to denote the angular momentum of the individual particles and F to denote the total angular momentum of the two particles.

the scattering lengths we can calculate two interaction coefficients

$$\begin{aligned} c_0 &= \frac{4\pi\hbar^2}{m} \frac{a_0 + 2a_2}{3} = 100.84a_0 \frac{4\pi\hbar^2}{m} \\ c_2 &= \frac{4\pi\hbar^2}{m} \frac{a_0 - a_2}{3} \approx -4.7 \times 10^{-3}c_0. \end{aligned} \quad (2.23)$$

Here c_0 represents a spin-independent interaction strength that depends only on the total density while c_2 is a spin-dependent energy that is relevant only where there is non-zero density of both atoms in $m_F = \pm 1$ and is much smaller than the spin-independent energy. Similar to the case of single component BECs, the dynamics of multiple component BECs is governed by a spinor GP equation (see [9, 25]). The spin-dependent interaction strength gives rise to processes like coherent spin-mixing oscillations and domain formation and coarsening which was previously studied in the our lab [29].

The time scale at which interactions become relevant is set by the interaction energies $n|c_i|$. The most noticeable effect of interactions in our system is the density profile of the condensate and its anisotropic expansion after it is released from a trap which I will describe in the following sections. For the typical densities and timescales of our experiments as well as the relatively high magnetic fields that we operate at, we do not observe noticeable effects from interactions in the dynamics of the system and in the remaining chapters I will describe the dynamics of the BEC using single particle physics (i.e. the regular time-dependent Schrödinger equation).

2.2.3 Thomas-Fermi approximation

For systems with large N , the interaction term in the GP equation is very large compared to the kinetic energy². As the kinetic energy becomes less important we enter the Thomas-Fermi (TF) regime where the energy of the system is given only by the external potential and the mean field energy and the GP equation is considerably simplified

$$[V(\mathbf{r}) + g|\psi(\mathbf{r})|\psi(\mathbf{r})|^2] \psi(\mathbf{r}) = \mu\psi(\mathbf{r}). \quad (2.24)$$

In the TF regime the density distribution of the condensate $n(\mathbf{r}) = |\psi(\mathbf{r})|^2$ reflects the shape of the external potential

$$n(\mathbf{r}) = g^{-1}[\mu - V(\mathbf{r})], \quad (2.25)$$

when $\mu - V(\mathbf{r}) > 0$ and is otherwise zero. For a harmonic confining potential (Equation 2.11) as is typical in our experiments we find that the length scale that characterizes the size of the condensate is the Thomas-Fermi radius

$$R_j = \sqrt{\frac{2\mu}{m\omega_j^2}}, \quad j = x, y, z. \quad (2.26)$$

The density of the condensate is described by an inverted parabola

$$n(\mathbf{r}) = \frac{\mu}{g} \left(1 - \frac{x^2}{R_x^2} - \frac{y^2}{R_y^2} - \frac{z^2}{R_z^2} \right). \quad (2.27)$$

²It can be shown that the ratio of kinetic energy to interactions scales like $N^{-4/5}$

as is shown in Figure 2a. By integrating over Equation 2.27 we find that

$$N = \frac{8\pi}{15} \frac{\mu}{g} R_x R_y R_z, \quad (2.28)$$

which allows to determine the number of atoms in the condensate based on the density profile. In practice, in-situ BECs are very dense which can lead to some technical difficulties when trying to image directly their density profiles (see Section 3.4) so instead our images are taken after the atoms are released from the trap and allowed to expand for some time. ~~In the next section I will discuss how the density profiles of atomic clouds are modified after they are released from a confining potential.~~

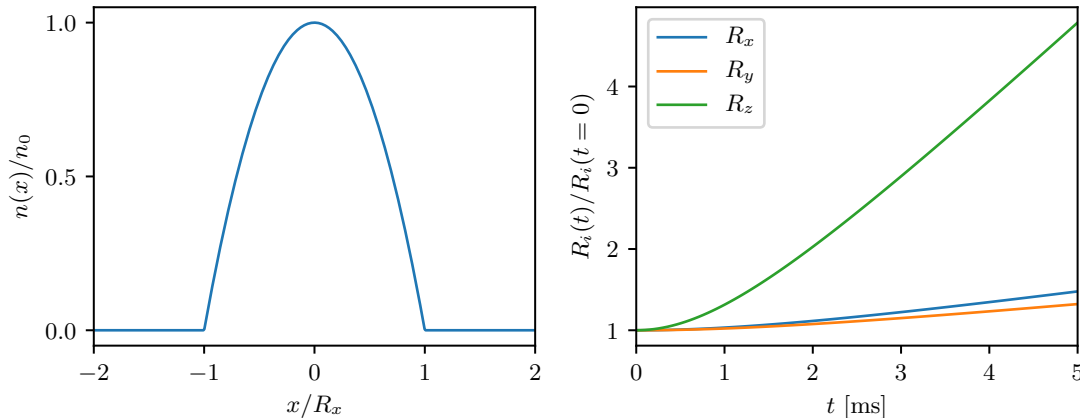


Figure 2: In the Thomas-Fermi regime where interactions are large compared to kinetic energy the density profile is determined by the external potential. **a.** Density profile along \mathbf{e}_x of a BEC in a harmonic potential. **b.** Interaction driven expansion of a BEC in time-of-flight for a trap with trapping frequencies $(\omega_x, \omega_y, \omega_z) = 2\pi(42, 34, 133)$ Hz obtained by numerically integrating Equation 2.30.

2.3 Density profiles

~~Most ultracold atoms experiments are probed by directly imaging the atoms~~ (e.g. with absorption imaging, Section 3.4). If the atoms are imaged in-situ we gain access to their spatial density profiles. If the atoms are released from the trap and allowed to expand in time of flight (TOF) we ~~gain access to~~ their momentum distribution. In this section, ~~I summarize the signatures in the density distributions of BECs and thermal atoms confined in a harmonic potential both in-situ and after TOF.~~

For the case of a BEC confined in a harmonic potential at zero temperature (no thermal fraction) and in the Thomas-Fermi regime discussed in Section 2.2.3, the in-situ density distribution is described by

$$\begin{aligned} n(\mathbf{r}) &= n_0 \left(1 - \frac{x^2}{R_x^2} - \frac{y^2}{R_y^2} - \frac{z^2}{R_z^2} \right) \\ &= \frac{15N}{8\pi R_x R_y R_z} \left(1 - \frac{x^2}{R_x^2} - \frac{y^2}{R_y^2} - \frac{z^2}{R_z^2} \right). \end{aligned} \quad (2.29)$$

Even though the BEC is in the motional ground state, it will expand during TOF as a consequence of interactions. The expansion can be determined using the time dependent GP equation. A detailed account of the procedure can be found in [27], the procedure relies on using the ansatz that the TF radii expand as

$$R_i(t) = \lambda_i(t) R_i(t=0), \quad (2.30)$$

where I assumed that the condensate is in the trap at $t = 0$ which implies that $\lambda_i(0) = 1$. The trap is then suddenly turned off at $t > 0$. If we insert the condensate wave function with TF radii given by Equation 2.30 into the time-dependent GP equation we find a series differential equations

$$\frac{d^2\lambda_i}{dt^2} = \frac{\omega_i^2}{\lambda_i \lambda_x \lambda_y \lambda_z} \quad (2.31)$$

which can be used to determine the density profile of the BEC in TOF. Alternatively, if the density profile of the BEC is known from an image, these relations can be used to back-propagate what the original TF radii of the confined condensate were. This is helpful for example to calculate the atom number in the condensate using Equation 2.28. Figure 2b shows the scaling factors λ_i as a function of TOF that were obtained by numerically integrating Equation 2.30 for a harmonic potential with frequencies close to those characterizing the optical dipole trap used in the lab.

For a thermal gas in a harmonic potential at temperatures higher than the level spacing $k_B T > \hbar\omega_{x,y,z}$ the density is given by [4]

$$n_{\text{th}}(\mathbf{r}) = \frac{1}{\lambda_{\text{th}}^3} g_{3/2}(z(\mathbf{r})) \quad (2.32)$$

where $z(\mathbf{r}) = \exp(\mu - V(\mathbf{r})/\mathbf{k}_B T)$, $V(\mathbf{r})$ is given by Equation 2.11, μ is the chemical potential and $g_j(z) = \sum_i z^i / i^j$ is the Bose function. The Bose function introduces effects of quantum statistics and compared to the Maxwell-Boltzmann distribution of distinguishable particles, the peak density of a Bose gas is increased by $g_{3/2}(z)/z$,

a phenomenon known as Bose-enhancement.

The distribution after TOF can be calculated considering that the trapped atoms fly ballistically from their position in the trap. An atom starting initially at the point \mathbf{r}_0 moves to the point \mathbf{r} after a time t if its momentum is given by $\mathbf{p} = m(\mathbf{r} - \mathbf{r}_0)/t$, and it can be shown that

$$\begin{aligned} n_{\text{tof}} &= \frac{1}{\lambda_{\text{th}}} \prod_{i=1}^3 g_{3/2} \left(\exp \left[\mu - \frac{m}{2} \sum_{i=1}^3 x_i^2 \left(\frac{\omega_i^2}{1 + \omega_i^2 t^2} \right) \right] \right) \\ &\approx \frac{1}{\lambda_{\text{th}}} g_{3/2} \left(\exp \left[(\mu - \frac{mr^2}{2t^2})/k_B T \right] \right) \end{aligned} \quad (2.33)$$

where the approximation in the second line is valid for $t \gg \omega_i^{-1}$. The temperature of the atoms can be estimated by looking at the wings of the density distribution after TOF. Even with the case of Bose enhancement, the density of the wings still decays exponentially as $\exp(-x_i^2/2\sigma_i^2)$. The temperature of the cloud can be determined using

$$\begin{aligned} k_B T &= \frac{m}{2} \left(\frac{\omega_i^2}{1 + \omega_i^2 t^2} \sigma_i^2 \right) \\ &\approx \frac{m}{2} \left(\frac{\sigma_i}{t} \right)^2 \end{aligned} \quad (2.34)$$

For partially condensed clouds the density profiles will be given by a combination of the thermal density profiles and the Thomas-Fermi density profile. Figure 3 shows the density distributions of atoms extracted from images taken after a 21 ms TOF and therefore the position is mapped to momentum. The images also nicely summarize some of the main features discussed in this Chapter. Above T_c the density

profile of the atoms is ~~described by~~ the thermal distribution (Equation 2.33). When $T < T_c$ a small peak in the center of the thermal distribution appears indicating condensation ~~and as~~. As temperature is decreased the fraction of atoms in the condensed state (and therefore the height of the peak) increases. ~~The density distribution of the condensed atoms is given by Equation 2.29,~~ where the TF radius increases due to interactions and the scaling factors can be found using Equation 2.30.

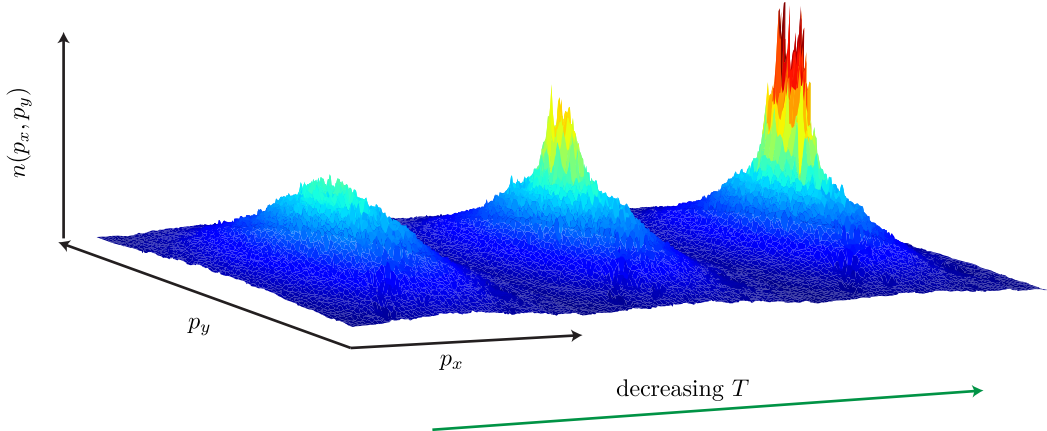


Figure 3: Momentum distribution of atoms near T_c after a 21 ms TOF. As the atoms ~~are cooled below~~ T_c a sharp peak in the momentum distribution appears indicating condensation.

Chapter 3: Manipulation and detection of ultra-cold atoms

All of the experiments described in this thesis were performed using ultracold clouds of ^{87}Rb . ~~In this Chapter I describe the techniques and interactions that make our experiments possible. This Chapter is not an extensive survey of atomic physics but rather covers the topics that are most relevant to my experiments. The references I included are helpful if the reader is interested in learning the details of the derivations or wants to expand on a given topic.~~

~~In Section 3.1 I start by describing the electronic structure of ^{87}Rb . In Sections 3.2 and 3.3 I describe atomic interactions with external fields that are necessary for the creation, manipulation and detection of ultracold atoms. First I review the interactions of atoms with magnetic fields and its application to magnetic trapping. Then I describe the foundations of atom-light interactions that make possible both laser cooling and trapping of atoms and give rise to Raman induced transitions. In Section 3.4 I discuss the resonant absorption imaging technique that we use to detect atoms after all our experiments are performed. Finally, in Section 3.5 I discuss coherent processes that use the magnetic and electric dipole interaction and are relevant to the experiments presented in Chapters 5, 6, and 8.~~

3.1 Electronic structure of ^{87}Rb

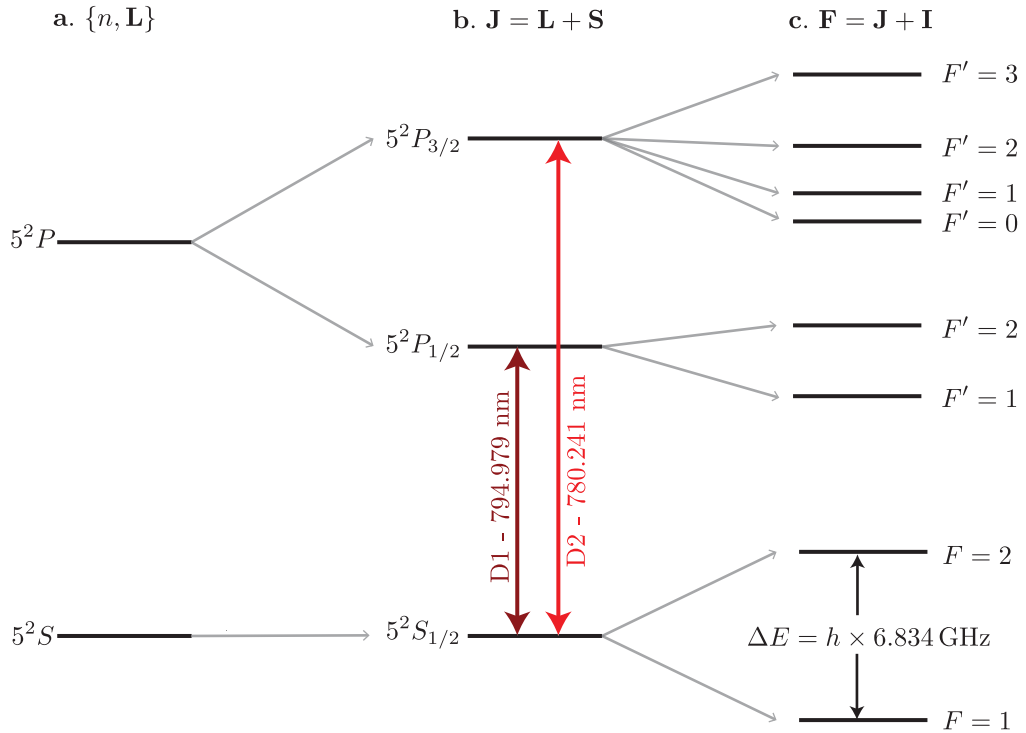


Figure 1: ^{87}Rb structure (not to scale). **a.** Ground and first excited state electronic configuration of ^{87}Rb given by the $\{n, \mathbf{L}\}$ quantum numbers. **b.** The interaction between the orbital angular momentum and the spin of the electron leads to the fine structure splitting of orbitals with $L > 0$. The splitting of the 5^2P line gives rise to the D1 and D2 lines. **c.** The interaction between the total angular momentum and the nuclear spin causes the fine structure levels to split further into states characterized by the quantum number F .

Rubidium is an Alkali metal (also Li, which exists in our vacuum chamber but was never used). Alkali metals correspond to the first group (leftmost column) of the periodic table and are characterized by having a single valence electron, which makes the description of their internal structure much simpler than that of other elements. The state of an electron in an atom is described by its angular

momentum $\hat{\mathbf{L}}$ and its spin $\hat{\mathbf{S}}$. Due to Pauli's exclusion principle there can not be two electrons with the same quantum numbers and in multi-electron atoms they tend to fill 'shells' of different angular momentum values, historically labeled by the letters S , P , D , F , ...¹ (corresponding to $L = 0, 1, 2, 3, \dots$). In particular, Rb has 4 filled shells and one electron in the $5S$ shell, where the number 5 corresponds to the principal quantum number n . Figure 1 shows the energy levels of the ground state $5S$ and its closest $5P$ orbital.

The relativistic treatment of the electron's motion gives rise to an interaction between the electron's intrinsic magnetic moment (the spin) $\hat{\mathbf{S}}$ and the orbital angular momentum $\hat{\mathbf{L}}$. This spin-orbit coupling interaction $\hat{H}_{\text{fs}} = A_{\text{fs}} \mathbf{L} \cdot \mathbf{S}$ causes the fine structure splitting of the electronic orbitals into levels with different total electronic angular momentum $\hat{\mathbf{J}} = \hat{\mathbf{L}} + \hat{\mathbf{S}}$. Figure 1b shows the $5^2S_{1/2}$, $5^2P_{1/2}$ and $5^2P_{3/2}$ electronic configurations that arise from this splitting, where I used the spectroscopic notation $n^{2S+1}L_J$ that indicates the values of the relevant quantum numbers. For S ($L = 0$) orbitals, $J = 1/2$ is the only possible value and the levels are not split. For the P orbital ($L = 1$) and a single electron with $S = 1/2$, J can be $1/2$ or $3/2$ and the P orbital splits into two levels. The $5^2S_{1/2} \rightarrow 5^2P_{1/2}$ is known as the D1 line and has wavelength $\lambda = 794.979 \text{ nm}$ and $5S_{1/2} \rightarrow 5P_{3/2}$ transition is known as the D2 line and has $\lambda = 790.241 \text{ nm}$ [30].

The atomic level structure gets further modified by the magnetic interaction of the electron with the nuclear spin \mathbf{I} . This is another kind of spin-orbit interaction

¹These terms were used to describe the lines in the emission spectra when they were first discovered. S stands for sharp, P for principal D for diffuse and F for further noted

that gives rise to the hyperfine splitting of the atomic levels which can be described by the Hamiltonian $\hat{H}_{\text{hfs}} = A_{\text{hfs}} \mathbf{I} \cdot \mathbf{J}$. A complete derivation of \hat{H}_{hfs} can be found in [31]. The hyperfine levels correspond to different values of the total angular momentum $\hat{\mathbf{F}} = \hat{\mathbf{J}} + \hat{\mathbf{I}}$. For ^{87}Rb $I = 3/2$ [30] which results in the level structure shown in Figure 1c, where the ground state is split into two levels with total angular momentum $F = 1$ and $F = 2$.

3.2 Interaction between atoms and magnetic fields

Atoms have an intrinsic magnetic moment that is given by the sum of nuclear and electronic moments

$$\hat{\boldsymbol{\mu}} = -\frac{\mu_B}{\hbar}(g_S \hat{\mathbf{S}} + g_L \hat{\mathbf{L}} + g_I \hat{\mathbf{I}}) \quad (3.1)$$

where μ_B is the Bohr magneton and g_S , g_L and g_I are the ‘ g -factors’ corresponding to the spin, orbital and nuclear angular momentum. In the presence of an external magnetic field \mathbf{B} , the internal levels of an atom get modified due to the Zeeman [32] interaction

$$\hat{H}_{\text{Zeeman}} = -\hat{\boldsymbol{\mu}} \cdot \mathbf{B}. \quad (3.2)$$

If the energy shift due to the Zeeman interaction is small compared to the hyperfine splitting then F is a good quantum number and we can write

$$\hat{H}_{\text{Zeeman}} = \frac{\mu_B g_F}{\hbar} \hat{\mathbf{F}} \cdot \mathbf{B} \quad (3.3)$$

where g_F is the hyperfine Landé g -factor and is given by

$$g_F = g_J \frac{F(F+1) - I(I+1) + J(J+1)}{2F(F+1)} + g_I \frac{F(F+1) + I(I+1) - J(J+1)}{2F(F+1)}, \quad (3.4)$$

and

$$g_J \approx 1 + \frac{J(J+1) + S(S+1) - L(L+1)}{2J(J+1)}. \quad (3.5)$$

is the Landé g -factor associated to the total electronic angular momentum J . The total energy shifts can be calculated by diagonalizing the full atomic Hamiltonian including the fine and hyperfine structure terms. Figure 2 shows the energies of the $|m_F\rangle$ levels in the $F = 1$ and $F = 2$ manifolds of the $5^2S_{1/2}$ electronic ground state of ^{87}Rb as a function of magnetic field. If the magnetic field is small then the Zeeman term can be treated as a perturbation to the atomic Hamiltonian and the energy split is linear with the magnitude of the field $E_{m_F} = g_F \mu_B m_F B$, what is known as the ‘linear Zeeman regime’ where F and $|m_F\rangle$ are good quantum numbers. In contrast, in the ‘Pachen-Back regime’ at large magnetic fields² the Zeeman term dominates over the fine and hyperfine terms and therefore the good quantum numbers of the system are J and m_J . Our experiments typically operate in an intermediate regime ($B \sim 10 - 30$ G, the gray box in Figure 2) where the energy of $|m_F = 0\rangle$ gets a small shift in energy that is quadratic in B . For atoms in $F = 1$ we define this quadratic Zeeman shift as $\epsilon = E_0 - (E_{+1} - E_{-1})/2$, where E_{m_F} is the Zeeman shift for state $|m_F\rangle$.

²A couple orders of magnitude larger than the fields we operate at.

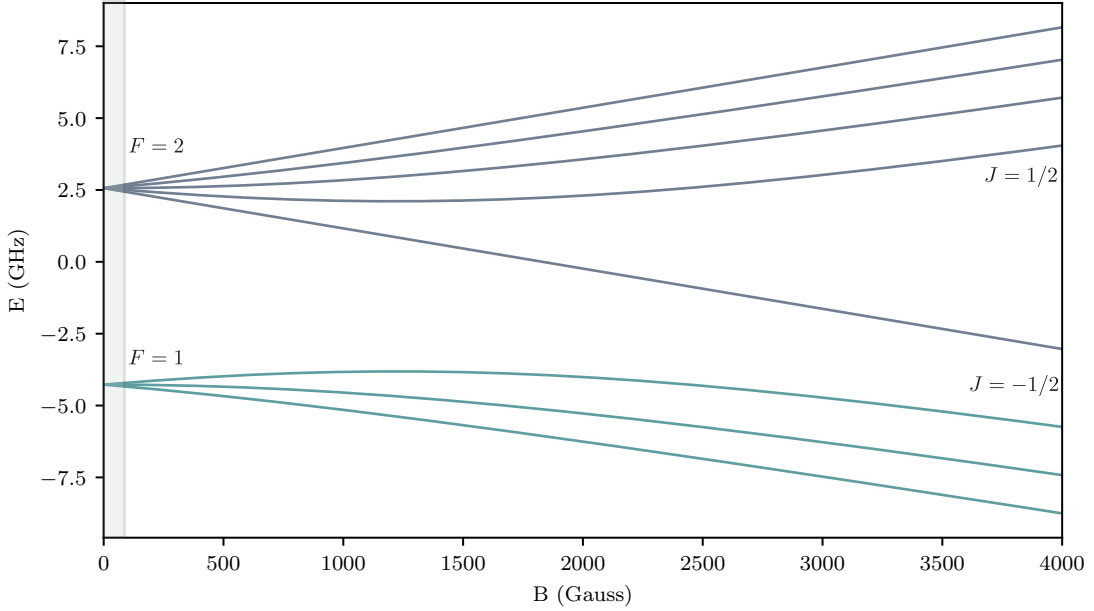


Figure 2: Zeeman splitting of the $5^2S_{1/2}$ manifold of ^{87}Rb . At small magnetic fields F and $|m_F\rangle$ are good quantum numbers describing the system and at large magnetic fields (Pachen-Back regime) the states are described by the J and m_J . Our experiments operate in the regime marked by the small gray box ($B < 35$ G).

For the particular case of states with $J = 1/2$ (like the ground state of Alkalies), the Zeeman energies can be found analytically using the Breit-Rabi formula [33]

$$E_{m_F} = -\frac{1}{2(2I+1)} + \frac{\mu_B g_I m_F B}{\Delta E_{\text{hf}}} + \frac{1}{2} \sqrt{1 + \frac{4m_F}{2I+1}x + x^2}, \quad (3.6)$$

where $\Delta E_{\text{hf}} = A_{\text{hf}}(J + 1/2)$ and $x = (g_J - g_I)\mu_B B_z / \Delta E_{\text{hf}}$.

3.2.1 Magnetic trapping

The sign of the Zeeman energy for different $|m_F\rangle$ states can be used to create state-dependent traps for atoms. In the lab, we implement magnetic traps using

quadrupole magnetic fields produced by a pair of anti-Helmholtz coils. The magnetic field near the center of the coils can be written as

$$\mathbf{B} = B'(x\mathbf{e}_x + y\mathbf{e}_y - 2z\mathbf{e}_z) + \mathbf{B}_0, \quad (3.7)$$

where \mathbf{B}_0 is a constant magnetic field, for simplicity I will assume that $\mathbf{B}_0 = B_0\mathbf{e}_z$.

The Zeeman Hamiltonian gives a trapping potential

$$\begin{aligned} U(\mathbf{r}) &= g_F\mu_B m_F B \\ &= g_F\mu_B m_F B' \sqrt{x^2 + y^2 + 4 \left(z - \frac{B_0}{2B'} \right)^2} \\ &\approx g_F\mu_B m_F B' \left(\rho + 2 \left| z - \frac{B_0}{2B'} \right| \right) \end{aligned} \quad (3.8)$$

where $\rho^2 = x^2 + y^2$ and the approximation on the second line is valid for small displacements from the trap center.

The sign of the magnetic moment determines which states can be trapped. For ^{87}Rb the $|F = 1, m_F = -1\rangle$, $|F = 2, m_F = 2, 1\rangle$ are magnetically trappable. The state $|F = 2, m_F = 0\rangle$ is also weakly magnetically trappable due to the quadratic Zeeman shift.

In addition to generating trapping potentials, we use quadrupole fields before imaging the atoms to generate state-dependent forces that separate the different $|m_F\rangle$ states in a similar way as the Stern-Gerlach (SG) experiment [34].

3.3 Interaction between atoms and electric fields

~~In this section, I will discuss the interaction between atoms and electric fields. After laying the foundations I will discuss applications using off-resonant electromagnetic radiation such as optical dipole traps and Raman transitions. I will not cover laser cooling which has been covered extensively in the literature [35, 36] and PhD theses from previous group members [37, 38].~~

In the presence of an electric field \mathbf{E} , an atom can become polarized and ~~therefore~~ its energy levels get modified by the Stark effect [39]. If the electric field is spatially uniform with respect to the atom's size we consider the electric field as a classical object and its effect on the atom can be described by the Hamiltonian [40]

$$\hat{H}_{\text{dip}} = -\hat{\mathbf{d}} \cdot \mathbf{E}, \quad (3.9)$$

where $\hat{\mathbf{d}} = -e \sum_j \hat{r}_j$ is the atomic dipole operator, e is the electron charge and \hat{r}_j are the position operators of the atom's electrons relative to the center of mass of the atom. This approximation, known as the dipole approximation, is valid for electromagnetic radiation when the wavelength is much larger than the size of an atom $\lambda \gg r_{\text{atom}}$ [41].

First I consider the simplified case a two-level system interacting with a coherent electromagnetic field $\mathbf{E} = \mathbf{E}^{(+)} e^{-i\omega t} + \mathbf{E}^{(-)} e^{i\omega t}$, where $\mathbf{E}^{(\pm)} = \hat{\epsilon} E^{(\pm)}$ are the positive/negative frequency components of the field, $\hat{\epsilon}$ the polarization, and ω is the angular frequency. It can be shown sing second-order perturbation theory that the

shift in energy of the ground state is

$$\begin{aligned}\Delta E_g &= -\frac{2\omega_{eg}|\langle g| \hat{\epsilon} \cdot \mathbf{d} |e\rangle|^2 |E^{(+)}|^2}{\hbar(\omega_{eg}^2 - \omega^2)} \\ &= -\frac{1}{2}\alpha(\omega)E^2\end{aligned}\quad (3.10)$$

where $\omega_{eg} = (E_e - E_g)/\hbar$ is the angular frequency associated to the energy splitting of the two states and $\alpha(\omega)$ is a dynamic polarizability. Things are a bit more complicated with real atoms though, and we need to take into account all the atomic levels. Furthermore, there are degeneracies associated to the different angular momentum states as well as different light polarizations so we have to be more careful with the orientation of the atom and the field. To take these effects into account one can introduce a generalization of the polarizability [41, 42] which takes the form

$$\begin{aligned}\alpha_{\mu\nu}(\omega) &= \sum_j \frac{2\omega_{jg} \langle g| d_\mu |e_j\rangle \langle e_j| d_\nu |g_j\rangle}{\hbar(\omega_{jg}^2 - \omega^2)} \\ &= \sum_{F', m_{F'}} \frac{2\omega_{F'F} \langle F, m_F| d_\mu |F', m_{F'}\rangle \langle F', m_{F'}| d_\nu |F, m_F\rangle}{\hbar(\omega_{F'F}^2 - \omega^2)}.\end{aligned}\quad (3.11)$$

Here $|e_j\rangle$ represent the excited states and $\omega_{jg} = (E_j - E_g)/\hbar$ and the expression in the second line corresponds to the polarizability of the hyperfine levels of an atom in the ground state $|F, m_F\rangle$ coupled to excited states $|F', m_{F'}\rangle$. We can therefore write an effective Hamiltonian for the Stark shift as

$$\hat{H}_{\text{Stark}} = -\alpha_{\mu\nu}(\omega)E_\mu^{(+)}E_\nu^{(-)}. \quad (3.12)$$

The polarizability is a rank-2 tensor operator and can be represented by 3 irreducible tensor operators (see [41] for a complete derivation). In the limit of small magnetic fields so that F and $|m_F\rangle$ are good quantum numbers describing the state of the atom $|n, F, m_F\rangle$ the dipole Hamiltonian in this representation takes a convenient form

$$\begin{aligned}\hat{H}_{\text{Stark}} = & \alpha^{(0)}(\mathbf{E}^{(-)} \cdot \mathbf{E}^{(+)}) + i\alpha^{(1)}(\mathbf{E}^{(-)} \times \mathbf{E}^{(+)}) \cdot \hat{\mathbf{F}} \\ & + \alpha^{(2)} E_i^{(-)} E_j^{(+)} \left(\frac{1}{2}(F_i F_j + F_j F_i) - \frac{1}{3} \hat{\mathbf{F}}^2 \delta_{i,j} \right) \Big],\end{aligned}\quad (3.13)$$

where $\alpha^{(0)}$, $\alpha^{(1)}$ and $\alpha^{(2)}$ are the scalar, vector and tensor polarizabilities respectively and $\hat{\mathbf{F}}$ is the total angular momentum operator. For all our experiments $\alpha^{(2)}$ is very small so I ~~will~~ limit the discussion to the effect of the first two terms. The scalar term is responsible for the dipole force that allow us to trap atoms using off-resonant light and the vector component is necessary for engineering spin-orbit coupling and other spin-dependent potentials through two-photon processes. ~~Finally,~~ I want to emphasize that it is because of the fine and hyperfine structure that the treatment using a tensor polarizability is necessary and the vector and tensor polarizabilities arise.

3.3.1 Scalar polarizability

The scalar polarizability takes the form

$$\alpha^{(0)} = \sum_j \frac{2\omega_{jg} |\langle g | \mathbf{d} \cdot \hat{\epsilon} | e_j \rangle|^2}{\hbar(\omega_{jg}^2 - \omega^2)},\quad (3.14)$$

where the matrix element can be expressed in terms of the Clebsch-Gordan coefficients and the reduced matrix element using the Wigner-Eckart theorem [43]. For the ground state of an Alkali atom ($J = 1/2$) and if the detuning is large compared to the hyperfine splitting the expression above gets simplified to

$$\alpha^{(0)} \approx \sum_{J'} \frac{2\omega_{JJ'} |\langle J = 1/2 | \mathbf{d} | J' \rangle|^2}{3\hbar(\omega_{JJ'}^2 - \omega^2)}. \quad (3.15)$$

Due to the second order-perturbation theory treatment, the scalar polarizability can be interpreted as arising from a two-photon process where the atom absorbs an off-resonant (virtual) photon and then returns to its initial state by emitting a photon.

The dipole matrix elements needed to compute the polarizability are related to the transition scattering rate via Fermi's golden rule [41, 43]

$$\Gamma_{JJ'} = \frac{\omega_{JJ'}^2}{3\pi\epsilon_0\hbar c^3} \frac{2J+1}{2J'+1} |\langle J | \mathbf{d} | J' \rangle|^2, \quad (3.16)$$

and combining this with the expression for the intensity of the electric field $I(\mathbf{r}) = 2\epsilon_0 c |\mathbf{E}(\mathbf{r})|^2$ it can be shown that the energy of the ground state manifold is shifted by

$$U(\omega, \mathbf{r}) = -\frac{\pi c^2 I(\mathbf{r})}{2} \left[\frac{\Gamma_{D1}(1 - qg_F m_F)}{\omega_{D1}^3} \left(\frac{1}{\omega + \omega_{D1}} - \frac{1}{\omega - \omega_{D1}} \right) + \frac{2\Gamma_{D2}(1 + qg_F m_F)}{\omega_{D2}^3} \left(\frac{1}{\omega + \omega_{D2}} - \frac{1}{\omega - \omega_{D2}} \right) \right], \quad (3.17)$$

where $q = 0, \pm 1$ for linearly and circularly polarized σ^\pm light and only the the most significant contribution from the closest transitions (the D1 and D2 lines) are included. Here $U(\mathbf{r})$ is related to the real part of the polarizability which is ~~in fact~~ a complex valued number. So far I have only considered a real valued polarizability by assuming the excited states have an infinitely long lifetime. However, in reality the atom can spontaneously emit photons and decay. This exponential decay can be accounted for by adding an imaginary contribution to the energies $\omega_D \rightarrow \omega_D + i\Gamma_D \omega^3 / \omega_D^3$ of the D1 and D2 transitions [44]. The scattering rate is related to the imaginary part of the polarizability and is given by

$$\Gamma(\omega, \mathbf{r}) = \frac{\pi c^2 I(\mathbf{r})}{2\hbar} \left[\frac{\Gamma_{D1}\omega^3}{\omega_{D1}^6} \left(\frac{1}{\omega + \omega_{D1}} - \frac{1}{\omega - \omega_{D1}} \right)^2 + \frac{2\Gamma_{D2}\omega^3}{\omega_{D2}^6} \left(\frac{1}{\omega + \omega_{D2}} - \frac{1}{\omega - \omega_{D2}} \right)^2 \right] \quad (3.18)$$

The energy shift $U(\omega, \mathbf{r})$ is a conservative term and is related to dipole trapping, while the scattering term $\Gamma(\omega, \mathbf{r})$ is dissipative and is important for laser cooling. In the context of engineering potentials for ultracold atoms with off-resonant light, the scattering is translated into heating because every time an atom emits a photon with angular frequency ω_L it gets a recoil momentum $\hbar\mathbf{k}_L$. If the frequency ω satisfies the relation $\omega + \omega_D \gg \omega - \omega_D$, as is often the case, we can neglect the terms proportional to $1/(\omega + \omega_D)$, an approximation typically known as the rotating wave approximation (RWA). If the RWA is valid then the frequency dependence of both the energy shifts and the scattering rates will be given by the detuning from the D1 and D2 transitions.

3.3.1.1 Optical trapping

One important application of the scalar light-shift is to create optical traps for clouds of ultracold atoms. An optical field with non-uniform spatial intensity generates traps (and anti-traps) for the atoms which experience a force proportional to the intensity gradient $F_{\text{dip}} = -\nabla U(\mathbf{r})$. The attractive or repulsive nature of the trap depends on the sign of $U(\mathbf{r})$ which is determined by the sign of the detuning (blue-detuned traps are repulsive and red-detuned traps are attractive). The production of BECs in our lab relies on the use of focused Gaussian laser beams of wavelength $\lambda = 1064 \text{ nm}$. The intensity profile of a focused Gaussian beam propagating along \mathbf{e}_z is given by

$$I(x, y, z) = \frac{2P}{\pi\omega^2(z)} e^{-\frac{x^2+y^2}{\omega^2(z)}} \quad (3.19)$$

where P is the total power of the beam and the $1/e^2$ radius is given by $w(z) = w_0\sqrt{1+z^2/z_R^2}$ where the minimum radius w_0 is known as the waist and $z_R = \pi\omega_0^2/\lambda$ is the Rayleigh range. If the extent of an atomic cloud is small compared to the size of the beam we can perform a Taylor expansion around $\mathbf{r} = 0$ to obtain a harmonic trapping potential

$$U(\mathbf{r}) = -U_0 \left(1 - 2\frac{x^2 + y^2}{\omega_0^2} - \frac{z^2}{z_R^2} \right). \quad (3.20)$$

The oscillation frequencies of the trap along the radial direction are $\omega_r = (4U_0/m\omega_0^2)^{1/2}$ and along the axial direction $\omega_z = (2U_0/mz_R)^{1/2}$. The beam waist is usually much smaller than the Rayleigh range ($\omega_0 \sim 50 - 150 \mu\text{m}$ for my experiments) and therefore the trap is much stronger along the axial direction. To get around this we use a

‘crossed’ dipole trap which is formed by a combination of two cross-polarized³ and frequency shifted focused Gaussian beams propagating along perpendicular directions, ensuring that we get good confinement of atoms along all spatial directions.

3.3.2 Vector polarizability and effective magnetic fields

The general expressions for the vector polarizability are quite complicated and depend both on reduced matrix elements and Wigner $6 - j$ symbols (see [41] for example for the complete expressions). For the particular case of Alkali atoms and for large detuning compared to the hyperfine splitting, the vector polarizability takes a simplified form [13]

$$\alpha^{(1)} = \frac{2\Delta_{fs}\alpha^{(0)}}{3(\tilde{E} - \hbar\omega)} \quad (3.21)$$

where $\Delta_{fs} = 3A_{fs}/2$ and $\tilde{E} = (2E_{D_1} + E_{D_2})$.

If we recall the Zeeman Hamiltonian introduced in Section 3.2, the term proportional to the vector polarizability in Equation 3.13 looks very similar to Equation 3.2 for an effective magnetic field

$$\mathbf{B}_{\text{eff}} = -\frac{i\hbar}{\mu_B g_J} \alpha^{(1)} (\mathbf{E}^* \times \mathbf{E}). \quad (3.22)$$

For the intensities that we typically operate at, the vector light shift is small and can be treated as a perturbation so the Hamiltonian resulting from this effective

³The beams are cross-polarized to avoid interference between them

magnetic field can be written as

$$\hat{H}_{\text{eff}} = \frac{\mu_B g_F}{\hbar} \mathbf{B}_{\text{eff}} \cdot \hat{\mathbf{F}} \quad (3.23)$$

3.3.2.1 Raman coupling

The vector light shift enables the realization of various spin dependent-potentials in the lab. In the experiments presented in Chapters 5 and 8 I used combinations of cross-polarized laser beams such that the total electric field $\mathbf{E}^* \times \mathbf{E} \neq 0$ could induce two-photon Raman transitions. A Raman transition is also a two-photon process but instead, we consider two ground states and an intermediate state that is off-resonantly coupled as is shown in Figure 3a. Due to the large detuning, the population transferred into the intermediate state is negligible and the state can be adiabatically eliminated [45]. In our experiments, we typically couple the $|m_F\rangle$ levels of the $F = 1$ manifold after applying a bias magnetic field such that ϵ is non-negligible.

Consider two laser beams counter-propagating along \mathbf{e}_x and with polarizations along \mathbf{e}_y and \mathbf{e}_z as is shown in Figure 3b. The electric field from the Raman beams is given by

$$\mathbf{E}(x, t) = E_a \cos(k_a x - \omega_a t) \mathbf{e}_y + E_b \cos(k_b x + \omega_b t) \mathbf{e}_z, \quad (3.24)$$

and consequently

$$\mathbf{E}^* \times \mathbf{E} = 2iE_aE_b \cos(2k_L x - \omega_{a,b}t) \mathbf{e}_x, \quad (3.25)$$

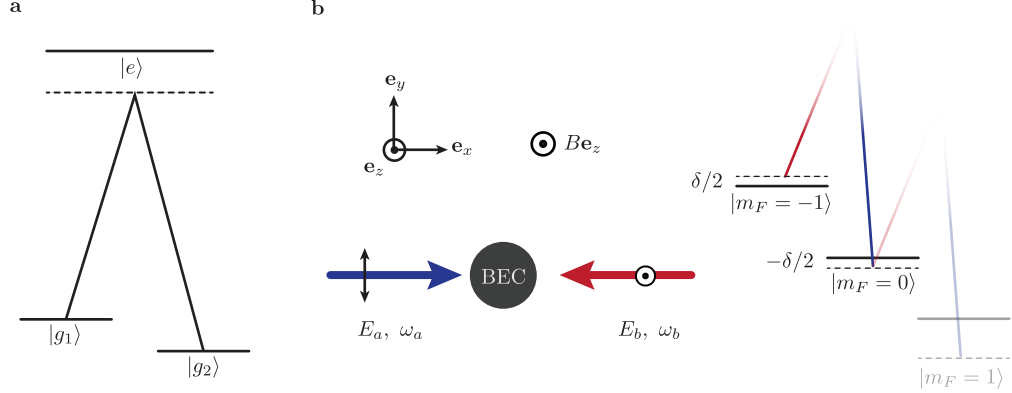


Figure 3: **a.** A Raman transition is a two photon process that couples two ground state through and intermediate far detuned state. **b.** We induce Raman transitions using a pair of cross-polarized laser beams whose and we set the difference in their angular frequencies close to the Zeeman splitting between two consecutive $|m_F\rangle$ states.

where $\omega_{a,b} = \omega_a - \omega_b$. The Raman Hamiltonian is given by

$$\hat{H}_R = \Omega \cos(2k_L x - \omega_{a,b} t) \hat{F}_x \quad (3.26)$$

where $\Omega = \alpha^{(1)} g_F E_a E_b / g_J \propto \sqrt{I_a I_b}$ is the Raman coupling strength. The geometry and wavelength of the Raman fields determine the natural units of the system: the single photon recoil momentum $k_L = 2\pi/\lambda_R$ and its associated recoil energy $E_L = \hbar^2 k_L^2 / 2m$, as well as the direction of the recoil momentum $\mathbf{k}_L = k_L \mathbf{e}_x$. For most experiments we tune to what is known as the ‘magic wavelength’ or tune-out wavelength [46] $\lambda_R = 790.034$ nm, at which the ground-state scalar polarizability vanishes and the scattering rate is reduced (Figure 4a,c). We occasionally had to tune away from the magic wavelength, for example when we were starving for laser power and wanted to increase our Raman coupling strength. An important metric for us is Raman coupling strength and Figure 4b shows its dependence on

wavelength; tuning closer to resonance allows us to decrease the laser intensity for the same intensities but comes with increased scattering rates and reduced lifetime as can be seen in Figure 4d which shows the decay in number of Raman dressed atoms as a function of time for different wavelengths.

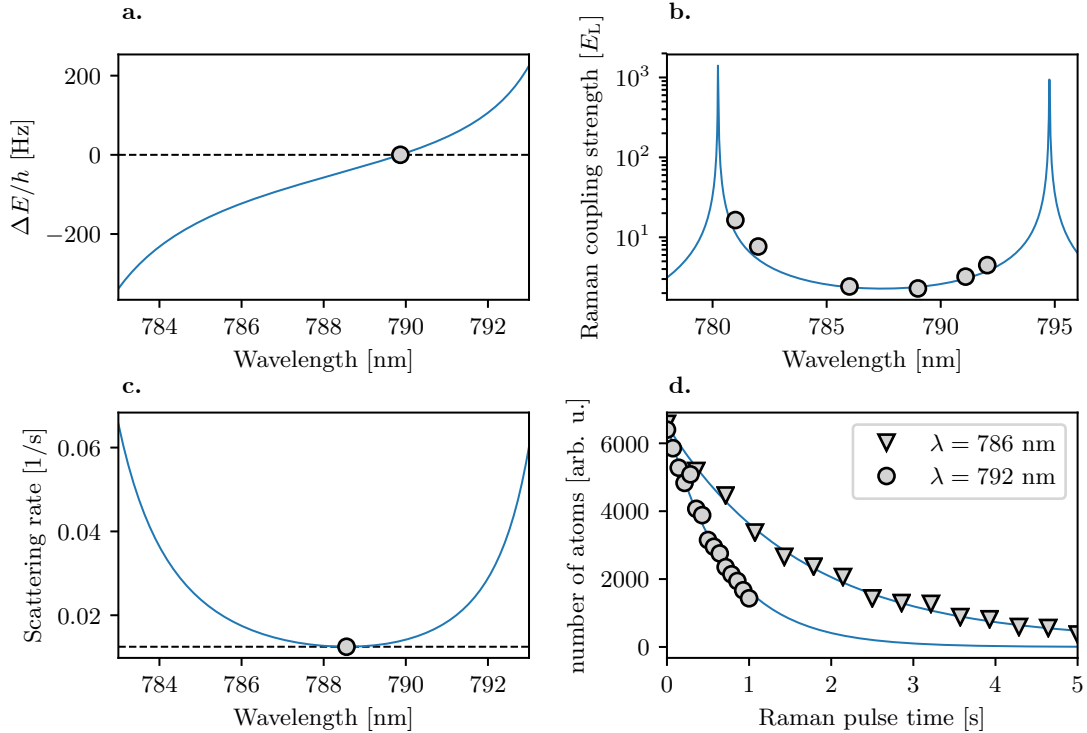


Figure 4: **a.** Scalar polarizability as a function of wavelength near the D1 and D2 lines of ^{87}Rb . We typically tune our Raman laser beams near the magic wavelength $\lambda = 790.034 \text{ nm}$. **b.** Raman coupling strength as a function of wavelength measured for a pair of Raman beams with waist $w_0 \sim 150 \mu\text{m}$ and powers of 50, 10 mW. **c.** Scattering rate as a function of wavelength, while it is not minimized at 790 nm its value is kept relatively low. **d.** Decay in number of Raman dressed atoms as a function of hold time for the same beam parameters as in **b.**. At $\lambda = 786 \text{ nm}$ the $1/e$ lifetime is $\tau = 1.64 \text{ s}$ and for $\lambda = 792 \text{ nm}$ it is reduced to $\tau = 0.72 \text{ s}$.

In a frame rotating with angular frequency $\omega_{a,b}$ corresponding to applying the unitary transformation $\hat{U}(t) = \exp(-i\omega_{a,b}t\hat{F}_z)$ and neglecting the fast terms rotating

at frequency $2\omega_{a,b}$ (applying a RWA) the transformed Hamiltonian is

$$\hat{U}^\dagger \hat{H}_R \hat{U} - i\hbar \hat{U}^\dagger \partial_t \hat{U} = \omega_{a,b} \hat{F}_z + \frac{\Omega}{2} \cos(2k_L x) \hat{F}_x - \frac{\Omega}{2} \sin(2k_L x) \hat{F}_y, \quad (3.27)$$

which describes a helically precessing magnetic field with period $\lambda_R/2$.

3.3.2.2 Spin-orbit coupling

The Raman Hamiltonian from Equation 3.27 can be ~~massaged a bit more~~⁴ to make it look like a spin-orbit coupled (SOC)⁴ Hamiltonian that is familiar to condensed matter physicists. If we apply a spin-dependent momentum boost which is described by the unitary operator $\hat{U}(k_L) = \exp(i2k_L x \hat{F}_z)$ the full Hamiltonian including the Raman coupling and the free particle energies is transformed ~~to~~^Y

$$\hat{H}_{SOC} = \frac{\hbar^2}{2m} (\hat{q}_x - 2k_L \hat{F}_z)^2 + \frac{\Omega}{2} \hat{F}_x + \delta \hat{F}_z + \hbar \epsilon \left(\mathbb{1} - \frac{\hat{F}_z^2}{\hbar^2} \right), \quad (3.28)$$

where $\delta = E_{-1} - \omega_{a,b}$. We can go from a 3 level system to an effective spin-1/2 system if we set $\omega_{a,b} = E_{-1} - E_0$ and consider a sizable quadratic Zeeman shift ϵ so the $|m_F = 1\rangle$ state can be adiabatically eliminated [47] giving an effective two-level system. After performing a global rotation $\hat{\sigma}_z \rightarrow \hat{\sigma}_y$, $\hat{\sigma}_y \rightarrow \hat{\sigma}_x$, and $\hat{\sigma}_x \rightarrow \hat{\sigma}_z$ of the Pauli matrices describing the pseudo-spin of the two-level system, the Hamiltonian becomes

$$\hat{H}_{SOC} = \frac{\hbar^2}{2m} (q_x - k_L \hat{\sigma}_y)^2 + \frac{\hbar}{2} \Omega \hat{\sigma}_z + \frac{\hbar}{2} \delta \hat{\sigma}_y \quad (3.29)$$

⁴Not to be confused with the spin-orbit coupling giving rise to the fine and hyperfine structure mentioned earlier, perhaps a better name could be spin-momentum coupling

which corresponds to a spin-orbit coupled Hamiltonian with an equal superposition of Rashba-type [21] ($\propto \hat{\sigma}_x k_y - \hat{\sigma}_y k_x$) and Dresselhaus-type [48] ($\propto -\sigma_x k_y - \sigma_y k_x$) SOC and effective magnetic field $\propto \Omega$ in the $\mathbf{e}_y - \mathbf{e}_z$ plane [19, 47]. In Chapter 8 I discuss the Rashba term in more detail and introduce a way of engineering a system with only Rashba-type SOC using multiple internal levels and Raman transitions.

3.4 Detection: Resonant absorption imaging

Ultracold atom experiments rely on optical imaging as the main method to probe and characterize the system. In our lab, we use resonant absorption imaging which uses a probing laser that is shone at the atomic cloud and then imaged into a camera. From the absorption of the light, we can infer properties from the atoms such as the number, temperature, integrated column density, and momentum distribution if we allow the clouds to expand.

Consider a laser beam with intensity $I(x, y, z)$ and angular frequency ω propagating along \mathbf{e}_z through a cloud of atoms with density $n(x, y, z)$ as is shown in Figure 5a. We define a (frequency-dependent) scattering cross-section $\sigma(\omega)$ which characterized the probability of an atom absorbing a probe photon and is given by the Lorentzian function

$$\sigma(\omega) = 3A_{eg} \frac{\pi^2 c^2}{\omega_0^2} \frac{1}{2\pi} \frac{\Gamma}{\delta^2 + \Gamma^2/4} \quad (3.30)$$

plotted in Figure 5b, where Γ is the scattering rate, ω_0 is the transition frequency, $\delta = \omega - \omega_0$ is the detuning, and A_{eg} is the Einstein coefficient associated to spontaneous

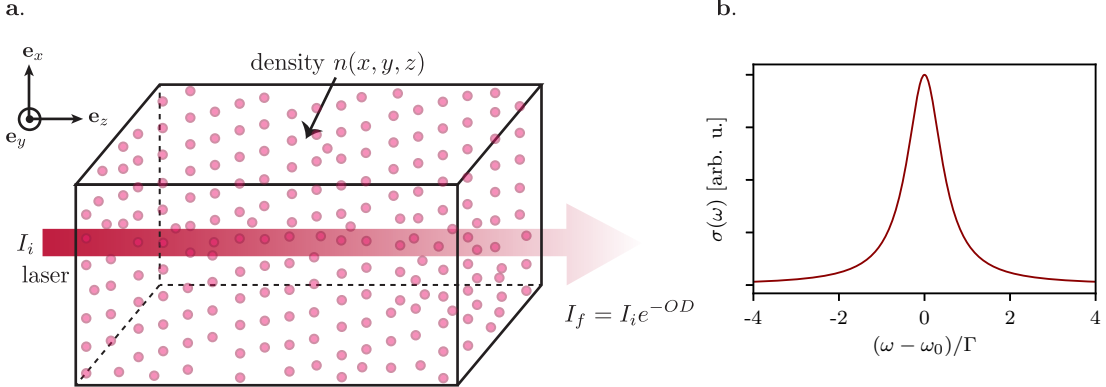


Figure 5: **a.** A laser beam traveling along e_z through a medium with density $n(x, y, z)$. The intensity decays exponentially with the integrated column density and the scattering cross section $\sigma\omega$. **b.** The scattering cross section has a Lorentzian line shape with a full width half maximum equal to Γ . [TODO: add real data on panel b if I have time.]

emission. As the beam travels through the cloud it ~~will be~~ absorbed and its intensity is reduced at a rate given by

$$\frac{dI}{dz}(x, y, z) = -n(x, y, z)\sigma(\omega)I(x, y, z). \quad (3.31)$$

In the limit of small intensities, we can integrate this expression over the thickness of the cloud and find that the intensity decays exponentially with the density and the scattering cross section

$$I(x, y, z) = I(x, y, 0)e^{-\int_0^z n(x, y, z')\sigma(\omega)dz'}, \quad (3.32)$$

where $OD = \int_0^z n(x, y, z')\sigma(\omega)dz'$ is the optical depth (OD) of the medium. If we

measure the OD of the cloud it is then straightforward to obtain the integrated column density $n(x, y)$, a result known as the Beer-Lambert law.

In the experiment we measure the optical depth of a cloud by imaging the probe into a CCD camera under two different conditions: first in the presence of atoms to measure the attenuated intensity $I_f = I(x, y, z)$ and then without any atoms to get a measure of the initial intensity $I_i = I(x, y, 0)$. The optical depth can then be computed as

$$OD = \ln \left(\frac{I_f}{I_i} \right). \quad (3.33)$$

Figure 6 show the different images used to compute the OD. In practice we take a third image of the background intensity I_{bg} and subtract it from the other two images.

3.4.1 High intensity absorption imaging

The use of the OD to infer the atomic density works well if we assume that the intensity of the probing laser is low such that the atoms mostly stay in the ground state. However, at high intensities a significant fraction of the atoms can become excited and effects such as stimulated emission of light have to be taken into account. As a result of this the scattering cross-section gets an additional dependence on intensity (see [49] for a complete derivation)

$$\sigma(\omega, I) = \sigma(\omega) \frac{1}{1 + I/I_{sat}}, \quad (3.34)$$

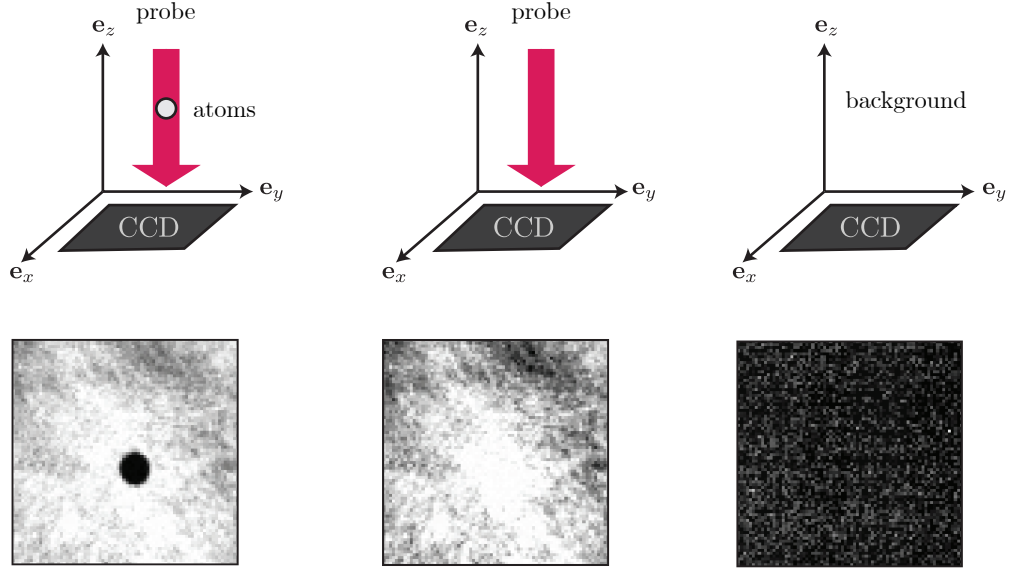


Figure 6: Resonant absorption imaging. An atomic sample is illuminated with a resonant probe whose intensity is later recorded on a CCD camera. Two additional images of the unabsorbed probe intensity and the background intensity are captured in order to reconstruct the optical density of the atoms.

where $I_{\text{sat}} = \pi h c \Gamma / 3 \lambda_0^3$ is the saturation intensity, and when $I = I_{\text{sat}}$ the population in the ground and excited state are equal. Integrating Equation 3.31 using the modified expression for $\sigma(\omega, I)$ gives

$$n(x, y)\sigma(\omega) = -\alpha^* \ln(I_f/I_i) + \frac{I_i - I_f}{I_{\text{sat}}}, \quad (3.35)$$

where I have also added an additional dimensionless parameter α^* which can account for imperfections in the imaging process (see [50]).

It is hard to reliably measure atomic clouds at low intensity when the OD is of the order of 3 or 4 (such as our BECs) and a significant fraction of the imaging light is absorbed. Due to the limited dynamic range of CCD cameras, the measured

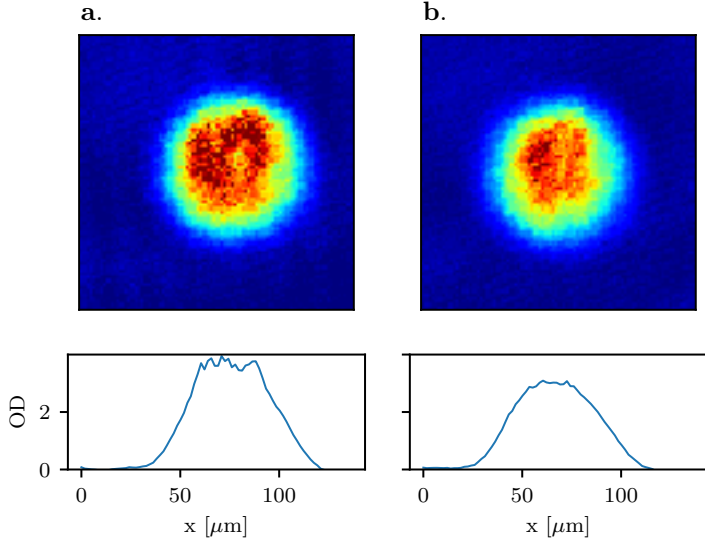


Figure 7: **a.** A BEC imaged at low intensity shows a ‘flat-top’ density profile. **b.** In order to recover the Thomas-Fermi profile it is necessary to image high density BECs with intensities larger than I_{sat} .

OD saturates resulting, for example, in imaging ‘flat-top’ BECs rather than the usual Thomas-Fermi distribution as shown in Figure 7. To get around this issue we typically image using intensities $I > I_{\text{sat}}$. In order to correctly compute the column density including saturation effects we need a conversion of I_{sat} from mW/cm² to counts per pixel on the CCD camera. We follow the procedure described in [50] to find the values of α^* and I_{sat} in counts per pixel. To learn about other effects such as the recoil momentum from the imaging light that could affect absorption images see [51].

3.5 Coherent manipulation

~~In this section, I describe quantum coherent processes that are driven within the electronic grounds state using the magnetic and electric dipole interactions de-~~

scribed in previous sections. We rely on these techniques both for state preparation and characterization of our system. In all of the cases I consider a system described by the Hamiltonian

$$\hat{H} = \hat{H}_0 + \hat{H}_I(t) \quad (3.36)$$

where \hat{H}_0 describes unperturbed atomic levels and $\hat{H}_I(t)$ is a time dependent interaction. For simplicity I consider only a two-level system

$$\hat{H}_0 = \hbar \begin{pmatrix} \omega_g & 0 \\ 0 & \omega_e \end{pmatrix} \quad (3.37)$$

where with $|g\rangle$ and $|e\rangle$ are the unperturbed ground and excited states where $\hbar\omega_i$ are the energies of the unperturbed states.

3.5.1 Rabi oscillations

First I consider an interaction term that oscillates with frequency ω close to the transition energy $\omega_{ge} = \omega_g - \omega_e$

$$\hat{H}_I = \hbar \begin{pmatrix} 0 & \Omega \cos(\omega t) \\ \Omega^* \cos(\omega t) & 0 \end{pmatrix}. \quad (3.38)$$

The coupling strength Ω here could be related to an electric dipole transition $\Omega \propto \langle g | \mathbf{d} \cdot \mathbf{E} | e \rangle^5$ or magnetic dipole $\Omega \propto \langle g | \boldsymbol{\mu} \cdot \mathbf{B} | e \rangle$ transition matrix element. The

⁵For our system intensities $\Gamma \gg \Omega$ and we don't observe Rabi oscillations from (single photon) electric dipole transitions.

state of the system at any given time is given by

$$|\Psi\rangle = c_g(t)e^{-i\omega_g t} |g\rangle + c_e(t)e^{-i\omega_e t} |e\rangle, \quad (3.39)$$

and substituting this expression into the time dependent Schrödinger equation we find that

$$\begin{aligned}\dot{c}_g(t) &= \frac{\Omega}{2} \left(e^{i(\omega-\omega_{ge})t} + e^{-i(\omega+\omega_{ge})t} \right) c_e \\ \dot{c}_e(t) &= \frac{\Omega^*}{2} \left(e^{i(\omega-\omega_{ge})t} + e^{-i(\omega+\omega_{ge})t} \right) c_g.\end{aligned}\quad (3.40)$$

We can apply a RWA if the term $\omega + \omega_{ge}$ is large compared to $\omega - \omega_{ge}$. The resulting coupled differential equations can be solved in a standard way by differentiating \dot{c}_e one more time and substituting \dot{c}_g . If we assume that at $t = 0$ the system is prepared in $|g\rangle$, the population in $|e\rangle$ describes what is known as a Rabi oscillation [52]

$$|c_e(t)|^2 = \frac{\Omega^2}{\Omega^2 + \delta^2} \sin^2 \left(\frac{\sqrt{\Omega^2 + \delta^2}}{2} t \right) \quad (3.41)$$

where $\delta = \omega - \omega_{ge}$ is a detuning and $\tilde{\Omega} = \sqrt{\Omega^2 + \delta^2}$ is known as the generalized Rabi frequency. The Hamiltonian after applying the RWA can be written as

$$\hat{H}_0 = \hbar \begin{pmatrix} -\delta/2 & \Omega/2 \\ \Omega^*/2 & \delta/2 \end{pmatrix}, \quad (3.42)$$

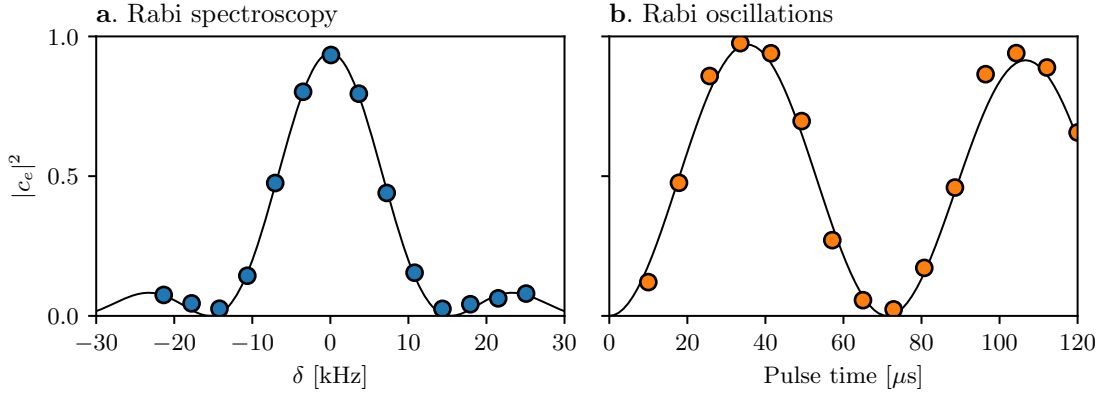


Figure 8: The Rabi cycle. Population transferred from $|F = 1, m_F = -1\rangle$ into $|F = 1, m_F = 0\rangle$ using an RF magnetic field with $\Omega = 7.1\text{ kHz}$. The markers indicate experimental data points and the lines correspond to fits to the model in Equation 3.41. **a.** Population transferred for a $60\text{ }\mu\text{s}$ pulse as a function of detuning δ . **b.** Population transferred as a function of time close to resonance.

and its eigenenergies correspond to $E_{\pm} = \pm\tilde{\Omega}/2$. Notice that the difference between the eigenenergies $E_+ - E_-$ is exactly equal to the frequency at which the populations in $|g, e\rangle$ oscillate, this will come up again in Chapter 5. Figure 8 shows an example of this process where we coupled an initial state $|g\rangle = |F = 1, m_F = -1\rangle$ to $|e\rangle = |F = 1, m_F = 0\rangle$ using a radio-frequency (RF) magnetic field with $\Omega = 7.1\text{ kHz}$. Figure 8a shows the population in $|e\rangle$ as a function of δ for a π pulse of duration τ such that $\Omega\tau = \pi$. The location of the peak in this curve is as a way to find the transition frequency (we use this method in Chapter 6). Figure 8b shows the population transferred into $|m_F = 0\rangle$ from $|m_F = -1\rangle$ as a function of time for $\delta \approx 0$; we typically look at the frequency of these Rabi oscillations to calibrate the coupling strength of an effective two-level system.

3.5.2 Adiabatic rapid passage

The Hamiltonian in Equation 3.42 can in principle be used to transfer all the population from the initial state $|g\rangle$ into $|e\rangle$ if we set the detuning of our oscillating field to $\delta = 0$ and apply a π pulse. Unfortunately ~~in the lab~~ we are susceptible to noise in both δ and Ω and pulsing is not the most reliable technique for state preparation. To transfer atoms within different $|F, m_F\rangle$ states within the $5^2S_{1/2}$ hyperfine manifold we use instead an adiabatic rapid⁶ passage (ARP) protocol which is based on the Landau-Zener model [53].

ARP relies on preparing dressed states; eigenstates of the atomic Hamiltonian (Equation 3.42) which I label using the symbols $|\pm\rangle$ and dynamically changing the detuning $\delta = \delta(t)$. We start at a large and negative detuning $\delta \ll -\Omega$ where the ground eigenstate $|-\rangle \approx |g\rangle$ and therefore by slowly turning Ω on we adiabatically prepare $|-\rangle$. We consider the rate of change in detuning $\partial_t \delta > 0$, and as δ increases the state decomposition of $|\pm\rangle$ changes. When $\delta = 0$ the dressed states correspond to equal superpositions of the bare states

$$|\pm\rangle = \frac{1}{2} (|g\rangle \pm |e\rangle), \quad (3.43)$$

and when $\delta \gg \Omega$ we have $|-\rangle \approx |e\rangle$. If the change in detuning is slow enough that the system can adiabatically follow the ground eigenstate $|-\rangle$ then at the end of this process the state can be successfully transferred from $|g\rangle$ into $|e\rangle$ by sweeping

⁶The term rapid is with respect to the spontaneous emission rate of the excited state being coupled.

the detuning. It can be shown that the fraction that does not adiabatically follow the ground state is given by the Landau-Zenner tunnel probability [41]

$$P_{\text{lost}} = \exp\left(-\frac{\pi\Omega^2}{2|\partial_t\delta|}\right). \quad (3.44)$$

In the limit of large coupling strength compared to the detuning sweep rate, or slow detuning sweep rate compared to the smallest energy gap ($\Omega \gg |\partial_t\delta|$) all the population adiabatically follows the ground state.

~~In the lab~~ we mostly use ARP with RF magnetic fields to transfer between different $|m_F\rangle$ states within the $F = 1$ manifold. We set the frequency of the field ω_{RF} so that it matches the Zeeman splitting between the $|m_F = -1\rangle$ and $|m_F = 0\rangle$ states for a target bias field $B_0\mathbf{e}_z$. We start with atoms in $|m_F = -1\rangle$ and at a bias field $B_i \approx B_0 - 380 \text{ mG}$ ($\delta \approx -30 \text{ kHz}$). We ramp an $\Omega = 20 \text{ kHz}$ RF field with angular frequency ω_{RF} in 50 ms. We then sweep the detuning by linearly changing the bias field in 50 ms. Finally, the RF field is abruptly turned off, projecting the RF eigenstates back into the $|m_F\rangle$ basis. In Figure 3.5.2 we set $\omega_{\text{RF}} = 23 \text{ MHz}$ and when the Zeeman splitting between $|m_F = -1\rangle$ and $|m_F = 0\rangle$ is equal to ω_{RF} we observe an equal superposition of both states and if the detuning is swept beyond resonance we can reliably prepare the $|m_F = 0\rangle$ state.

In general it is necessary to consider the eigenstates of the three-level RF

Hamiltonian for a full description of this process

$$\hat{H}_{\text{RF}} = \begin{pmatrix} -\delta & \Omega_{\text{RF}}/2 & 0 \\ \Omega_{\text{RF}}/2 & -\epsilon & \Omega_{\text{RF}}/2 \\ 0 & \Omega_{\text{RF}}/2 & \delta \end{pmatrix}, \quad (3.45)$$

but for large quadratic Zeeman shifts as is usually the case in our experiments we can only look at an effective two-level system.

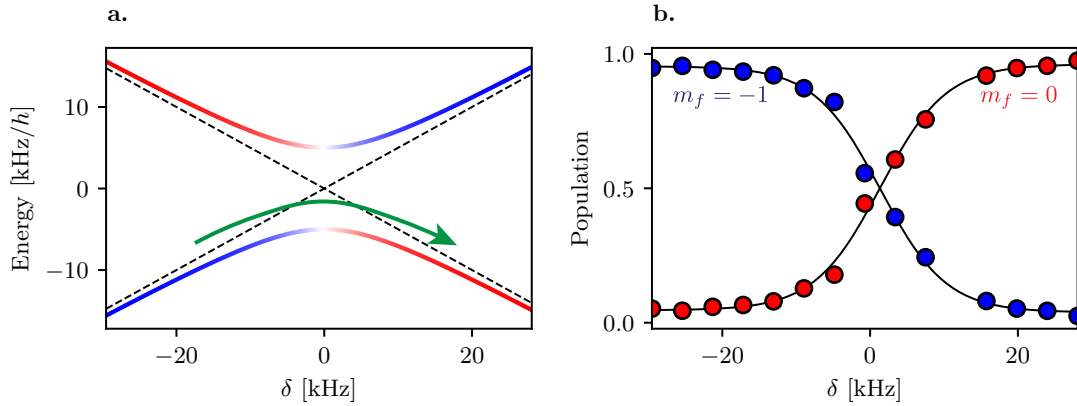


Figure 9: **a.** Eigenenergies and eigenstate decomposition of an RF dressed Hamiltonian for a two-level system (Equation 3.42) with $\Omega = 10$ as a function of detuning. The eigenstates are linear combinations of $|m_F = -1\rangle$ and $|m_F = 0\rangle$ (red and blue respectively). **b.** Population in the $|m_F\rangle$ states for different values of detuning

3.5.3 Magnetic field stabilization with microwave assisted partial transfer absorption imaging

Most experiments ~~in the lab~~ are performed in the $F = 1$ ground hyperfine manifold with some bias field $B_0 \mathbf{e}_z$ that shifts the energies of the different $|m_F\rangle$ states. Due to the linear dependence of the energies of the $|m_F = \pm 1\rangle$ and the

constant changes in the ambient magnetic field we use microwave assisted partial transfer absorption imaging (PTAI) to monitor and stabilize the magnetic field.

The method relies on transferring a small fraction of atoms into the $5^2S_{1/2}$ $F = 2$ manifold using an oscillating magnetic field with frequency close to the 6.8 GHz ground hyperfine splitting. The atoms in $F = 2$ can be imaged without the use of repump light and therefore minimally disturbing the remaining atoms in $F = 1$. We apply two microwave pulses for a total time τ with frequency $\omega_0 - \delta_{\pm}$ where $\delta_{\pm} = \pm 1/(2\tau)$. We typically set ω_0 equal to the Zeeman splitting between the $|F = 1, m_f = -1\rangle$ and $|F = 2, m_f = -2\rangle$ states at a target magnetic field and we set the coupling strength $\Omega_0 \ll 1/\tau$ such that only about 5% of the atoms are transferred by each pulse. We image the transferred atoms following each pulse using absorption imaging and from the measured densities we calculate the imbalance or error

$$n_{\text{imb}} = \frac{n(\delta_+) - n(\delta_-)}{n(\delta_+) + n(\delta_-)} \quad (3.46)$$

signal that is both insensitive to fluctuations in the number of atoms and linearly sensitive to changes in magnetic field⁷. We use this error signal both to monitor the magnetic field before performing experiments and to cancel long term drifts in the field. In most cases, we chose the states $|F = 1, m_F = -1\rangle$ and $|F = 2, m_f = -2\rangle$ as their relative energies are the most sensitive to changes in magnetic field. Figure 10a shows the number of atoms transferred by each microwave pulse for different values of bias magnetic field and Figure 10b shows the imbalance. The microwave frequency

⁷A single pulse on resonance is quadratically sensitive to detuning (see Equation 3.41)

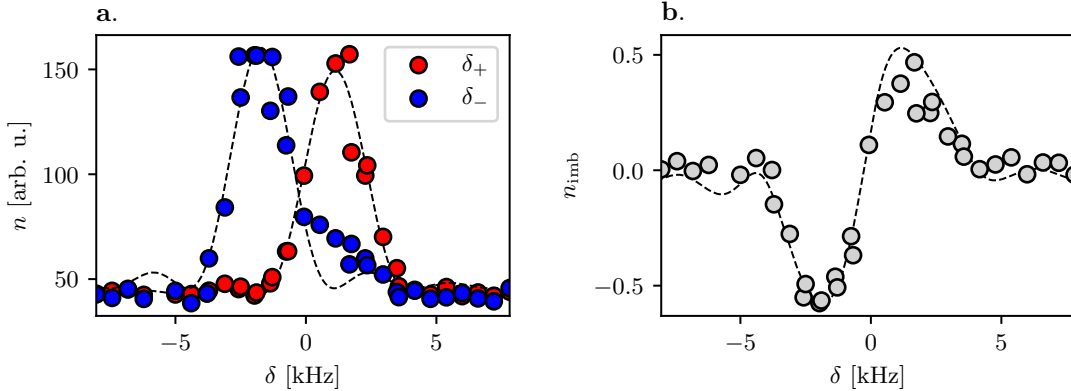


Figure 10: Magnetic field stabilization using microwave assisted PTAI. **a.** Population transferred into $|F = 2, m_F = -1\rangle$ from $|F = 1, m_F = -1\rangle$ as a function of bias magnetic field (global detuning δ). Each microwave pulse was $\tau = 250 \mu\text{s}$ and detuned by $\delta_{\pm} = \pm 1/(2\tau)$ transfer a small fraction of atoms from $|F = 1, m_F = -1\rangle$ into $|F = 2, m_F = -1\rangle$. **b.** Error signal calculated using the transferred atoms by each pulse. We lock the magnetic field to the $\sim 5 \text{ kHz}$ ($\sim 7 \text{ mG}$) wide linear portion of the signal.

ω_0 is on resonance with the $|F = 1, m_F = -1\rangle \rightarrow |F = 2, m_F = -2\rangle$ transition when both pulses transfer the same number of atoms.

In [54] we studied partial transfer absorption imaging as a minimally destructive technique for imaging ultracold atoms. See Chapter 6 for an alternative solution for dealing with magnetic field noise.

3.5.4 Ramsey interferometer

Now I consider a Ramsey interferometer [55], a setup that is relevant to Chapters 6 and 8. The interaction Hamiltonian is the same as in the previous section but rather than being on continuously it is pulsed on for a time $\tau = \pi/2\Omega$ (a $\pi/2$ pulse), the system is then let to evolve only under \hat{H}_0 for a variable time t_{dark} and finally

a second $\pi/2$ pulse is applied. Figure 11a illustrates this protocol: the $\pi/2$ pulses can be visualized as $\pi/2$ rotations on the Bloch sphere along \mathbf{e}_x that transform the initial state $|g\rangle \rightarrow (|g\rangle + |e\rangle)/\sqrt{2}$. For the duration of the dark time, the system rotates along the equator of the Bloch sphere (about the \mathbf{e}_z axis in general) by an angle δt_{dark} and finally the second pulse rotates the state along the \mathbf{e}_x axis again. The probability of measuring the excited state is related to the phase accumulated during the dark time is given by

$$|c_e(2\tau + t_{\text{dark}})|^2 = \left| \frac{\Omega\tau}{2} \right| \left[\frac{\sin(\delta\tau/2)}{\delta\tau/2} \right]^2 \cos^2 \left(\frac{\delta t_{\text{dark}}}{2} \right). \quad (3.47)$$

In a Ramsey interferometer the oscillation frequency is only determined by the detuning unlike the generalized Rabi frequency where the detuning adds in quadrature with Ω . The coupling strength dependence in the generalized Rabi frequency suppresses the effect of the detuning Ω becomes large compared to δ , something that will be relevant in Chapter 6. Additionally in Chapter 8 I rely on a variation of the Ramsey interferometer to perform quantum state tomography. Figure 11b shows an example of a Ramsey fringe as a function of detuning δ that we measured using two states coupled with $\Omega = 1$ kHz.

3.5.5 Floquet theory

The RWA has been used multiple times throughout this Chapter so that the Hamiltonian describing a driven system can effectively be viewed as time-independent. This approximation is valid most of the time for our experiments,

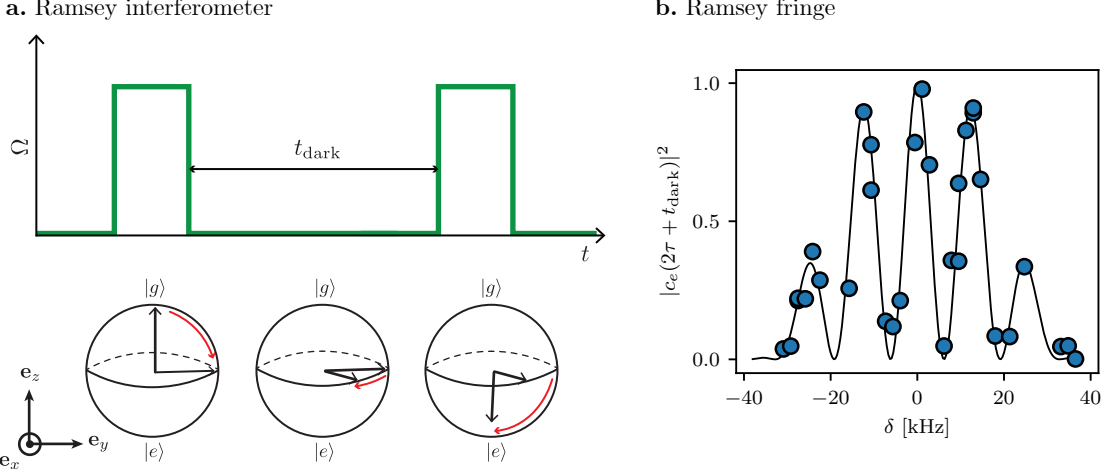


Figure 11: **a.** A Ramsey interferometer: Two $\pi/2$ pulses are separated by a time t_{dark} . The phase accumulated in the interferometer is equal to the detuning multiplied by the dark time. **b.** A Ramsey interference fringe obtained from coupling two levels using an RF field with $\Omega = 1 \text{ kHz}$. We applied a pair of $\tau = 25 \mu\text{s}$ pulses separated by a $50 \mu\text{s}$ wait and varied the detuning by changing the bias magnetic field.

however, if we want to give a complete description of a time periodic system Floquet theory can be helpful. I will give a brief overview of Floquet theory using a matrix approach that is particularly useful for numerical computations.

An arbitrary time periodic Hamiltonian $\hat{H}(t) = \hat{H}(t + T)$ can be written in terms of its Fourier components

$$\hat{H}(t) = \sum_{j=-\infty}^{\infty} \exp[ij\omega t] \hat{H}_j, \quad (3.48)$$

with $\omega = 2\pi/T$ and because \hat{H} and $\hat{H}_j = \hat{H}_{-j}^\dagger$ due to the Hermitian nature of \hat{H} . The eigenstates of the Hamiltonian can be written in terms of quasi periodic

functions⁸

$$|\psi_\epsilon(t)\rangle = \exp(-i\epsilon t/\hbar) \sum_{k=-\infty}^{\infty} \exp[-ik\omega t] |\psi_{\epsilon,k}\rangle \quad (3.49)$$

where the term ϵ is known as the quasi-energy. Inserting this expression into the time-dependent Schrödinger equation gives

$$\sum_k (\epsilon + \hbar\omega k) \exp[-k\omega t] |\psi_{\epsilon,k}\rangle = \sum_{j,j'} \exp[i(j-j')\omega t] \hat{H}_{j'} |\psi_{\epsilon,j}\rangle. \quad (3.50)$$

In order for the equality to be true we must have $j' - j = -k$ because the complex exponentials form an orthonormal basis and we can write

$$\epsilon |\psi_{\epsilon,k}\rangle = \sum_j \left(\hat{H}_{j-l} - \hbar\omega k \delta_{j,k} \times \hat{\mathbb{1}} \right), \quad (3.51)$$

where $\hat{\mathbb{1}}$ is the identity matrix. The expression can be recast into a matrix form

$$\epsilon \begin{pmatrix} \dots \\ |\psi_{\epsilon,-1}\rangle \\ |\psi_{\epsilon,0}\rangle \\ |\psi_{\epsilon,1}\rangle \\ \dots \end{pmatrix} = \begin{pmatrix} \hat{H}_0 + 2\hbar\omega & \hat{H}_1 & \hat{H}_2 & \dots & \dots \\ \hat{H}_{-1} & \hat{H}_0 + \hbar\omega & \hat{H}_1 & \hat{H}_2 & \dots \\ \hat{H}_{-2} & \hat{H}_{-1} & \hat{H}_0 & \hat{H}_1 & \dots \\ \dots & \hat{H}_{-2} & \hat{H}_{-1} & \hat{H}_0 - \hbar\omega & \hat{H}_1 \\ \dots & \dots & \hat{H}_{-2} & \hat{H}_{-1} & \hat{H}_0 - 2\hbar\omega \end{pmatrix}. \quad (3.52)$$

The quasienergies ϵ can be computed by truncating and then diagonalizing the matrix, and they are grouped into repeating manifolds separated in energy by

⁸Very much like Bloch wave functions

$\hbar\omega$. The quasienergies within a manifold can be interpreted as the eigenenergies of an effective time-independent Hamiltonian \hat{H}_{Fl} that describes the evolution of the system sampled stroboscopically at an integer number of driving periods, with the time evolution operator $\hat{U}(t_0, t_0 + T) = e^{-iT\hat{H}_{Fl}}$.

Floquet theory ~~played~~ an important role in the engineering of different dispersion relations for atoms in Chapters 5 and 8. I will give an example based on the experiments described in [56] (not included in this Thesis), where we considered a pair of Raman beams driving transitions between the $|F = 1, m_F\rangle$ states of the ground hyperfine manifold with two different frequencies $\omega_{-1,0}$ and $\omega_{0,+1}$ set to the $m_F = -1 \rightarrow m_F = 0$ and $m_F = 0 \rightarrow m_F = 1$ transitions. By performing independent RWAs with respect to each of these transitions we found that the system could be described by a magnetic Hamiltonian

$$\hat{H} = \frac{\hbar k^2}{2m} + \boldsymbol{\Omega}(x) \cdot \hat{\mathbf{F}} + \Omega_2 \hat{F}_{zz}^{(2)} \quad (3.53)$$

with helical effective magnetic field $\boldsymbol{\Omega}_1(x)/\Omega_1 = \cos(2k_R x)\mathbf{e}_x - \sin(2k_R x)\mathbf{e}_y$, an effective quadratic Zeeman shift $\Omega_2 = (\omega_{-1,0} - \omega_{0,1})/2$, and $\hat{F}_{zz}^{(2)}\hbar = \hat{F}_z^2/\hbar^2 - 2/3$ an element of the quadrupole tensor. The competing contributions between kinetic and magnetic ordering energies gave rise to different magnetic phases. Figure 12a. shows the ground branch of the dispersion relation for small $\Omega_1 < 4E_L$ (top) and large $\Omega_1 > 4E_L$ (bottom). As the value of Ω_2 was decreased, the magnetization in the system changed along with the location of the global minima in the dispersion. The experimental parameters Ω_1 and Ω_2 spanned a two-dimensional phase

diagram shown in Figure 3.53b that we experimentally mapped. The eigenenergies of Equation 12 are plotted in Figure 12c. However in order to get a good agreement between the experiment and the phase diagram we had use the full Floquet Hamiltonian which results in having modified parameters in Equation 3.53 $\Omega_2^{(\text{eff})} = \Omega_2 + \mathcal{O}(\Omega_1^2/\epsilon)$ (red dotted line in Figure 12b). Figure 12d shows three manifolds of Floquet quasienergies for this system, illustrating their periodic nature.

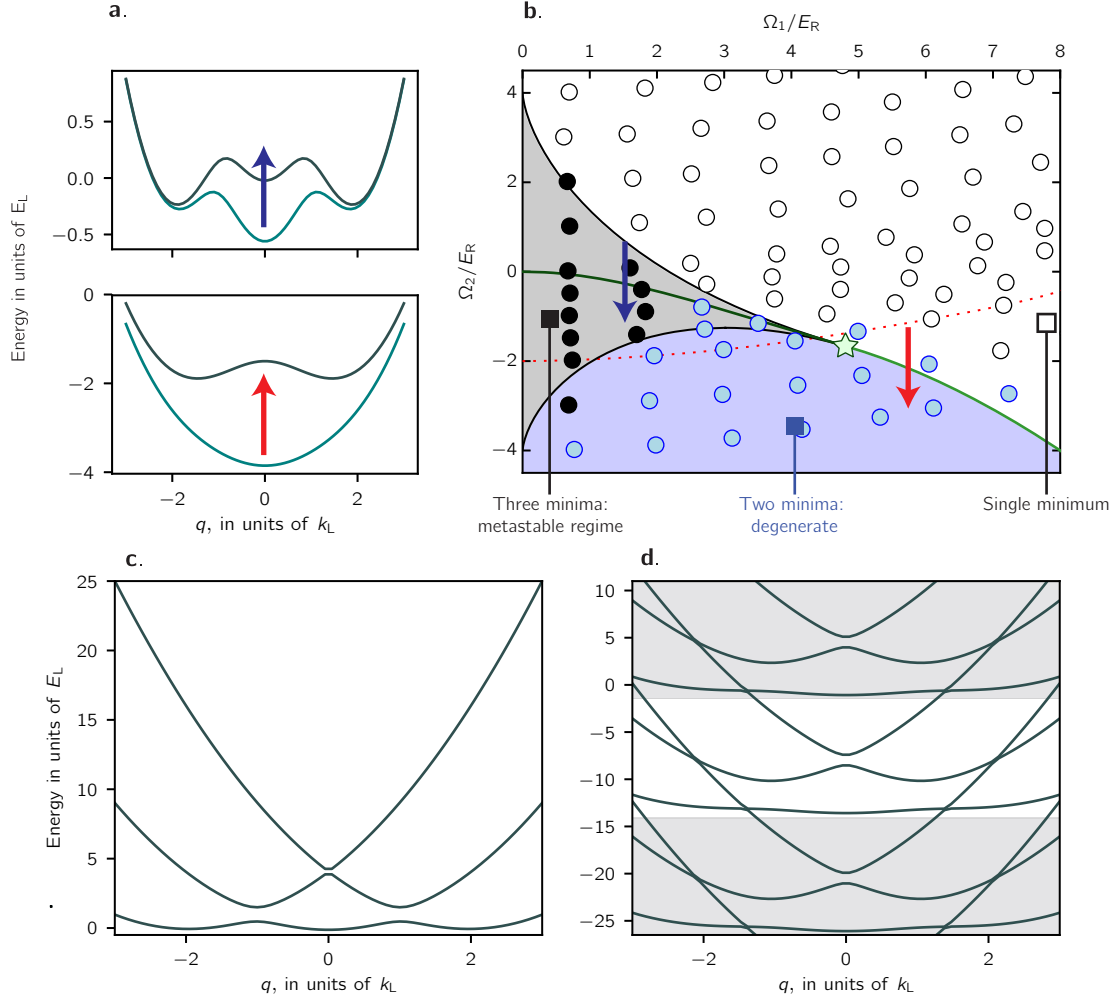


Figure 12: Magnetic phases of a spin-1 SOC system. **a.** Ground state energies of a spin-1 SOC system for $\Omega_1 = 1.5 E_L$ (top) and $\Omega_2 = 1.5 E_L$ (bottom). By changing Ω_2 we moved the location of the central minima. **b.** Phase diagram of a spin-1 SOC system. They green line corresponds to a line of phase transitions where the system goes from magnetized to unmagnetized. **c.** Dispersion relation of effective Hamiltonian computed for $\Omega_1 = 2 E_L$, $\Omega_2 = 0$. **d.** Floquet quasienergy dispersion relation for the same parameters. The magnitude of Ω_1 effectively modifies Ω_2 in the RWA Hamiltonian.